

FEASIBILITY STUDY OF AN ULTRA FAST GATED CAMERA TO IMAGE
BILIARY TREE EMBEDDED IN ADIPOSE TISSUE USING
LABORATORY PHANTOMS AND MONTE
CARLO SIMULATIONS

by

NIMIT PATEL

Presented to the Faculty of the Graduate School of
The University of Texas at Arlington in Partial Fulfillment
of the Requirements
for the Degree of

MASTER OF SCIENCE IN BIOENGINEERING

THE UNIVERSITY OF TEXAS AT ARLINGTON

December 2008

Copyright © by Nimit Patel 2008

All Rights Reserved

ACKNOWLEDGEMENTS

At the outset, I would like to express my sincere gratitude to all the people who helped me make this thesis possible.

It is difficult to overstate my gratitude to my supervisor, Dr. Hanli Liu. She gave inspiration throughout my work and guided and supported me in all the possible ways. During the course of the research, she provided me encouragement, sound advice, good teaching and many ideas to make my thesis better. Without her valuable suggestions, support and guidance this thesis would not have been possible.

I would like to thank Dr. Edward Livingston for believing in my abilities and giving me an opportunity to work on the clinically challenging problem. He always explained me the actual problems in the clinics very clearly. I owe my most sincere gratitude to Dr. George Alexandrakis for guiding me throughout the course of my thesis. I would also like to thank him for teaching courses on tissue optics and fluorescence microscopy which made the foundation for my thesis.

I thank my friends Vikram, Aniket, Yajuvendra and Zi-Jing for their valuable advice, friendly help and encouraging words. Lastly and most importantly, I wish to thank my parents, Urvashi and Lalit Patel who raised, supported, taught, loved and inspired me to earn things through hard work and sincerity. To them I dedicate this thesis.

November 26, 2008

ABSTRACT

FEASIBILITY STUDY OF AN ULTRA FAST GATED CAMERA TO IMAGE BILIARY TREE EMBEDDED IN ADIPOSE TISSUE USING LABORATORY PHANTOMS AND MONTE CARLO SIMULATIONS

Nimit Patel, M.S.

The University of Texas at Arlington, 2008

Supervising Professor: Dr. Hanli Liu

Every year, approximately 500,000 cholecystectomies are performed in US. As biliary tree structures are embedded in adipose tissue, they cannot be visualized directly by the surgeon, which causes inadvertent injuries to the common bile duct, vein and artery during a laparoscopic cholecystectomy. Thus there is an urge for an imaging modality which could see biliary tree structure through fatty tissue. Successful clinical implementation of an imaging system which could attain this goal would reduce surgical time, improve patient safety and minimize the risk of complications and expenses attributable to the current standard practice of intraoperative cholecystectomy.

It is hoped that the work presented here will contribute to the accomplishment of this important clinical goal.

I propose a novel time-gated imaging modality for the intraoperative localization of biliary tree structures by means of an ultra fast gated Intensified Charge Couple Device (ICCD) camera. I have done an exploratory study using Monte Carlo (MC) Simulations and laboratory phantom experiments. In the MC simulations the optical properties of bile and adipose tissue were used to mimic the actual clinical scenario. To check the effect of gate width on the performance of the camera, the MC simulations were repeated at two different gate widths (0.3 ns and 0.03 ns). To analyze sensitivity and spatial resolution of the proposed imaging technique, selected intensity profiles from the gated images/slices were fitted using a 'Lorentzian Function'. Full Width at Half Maximum (FWHM) and Contrast to Background Ratio (CBR) of the fitted Lorentzian curve were used to characterize spatial resolution and sensitivity of the camera, respectively. The MC simulations were performed in both transmission and reflectance mode to find the suitable illumination geometry for the clinical measurements. Comparison was done for the CBR and FWHM values using both illumination schemes and two gate widths. In addition, results of the MC simulations were validated through laboratory phantom experiments with an absorber at different depths within an intralipid solution. The next step is to further test the imaging system in the laboratory using actual bile as an absorber in phantom experiments and then in the operation room.

TABLE OF CONTENTS

ACKNOWLEDGEMENTS.....	iii
ABSTRACT.....	iv
LIST OF ILLUSTRATIONS.....	ix
LIST OF TABLES.....	xiii
Chapter	Page
1. INTRODUCTION.....	1
1.1 Biliary Tree and Anatomy	1
1.2 Gallstones	2
1.3 Cholecystectomy	3
1.4 Imaging Modalities	4
1.5 Motivation for Research	8
2. MONTE CARLO SIMULATIONS	10
2.1 Simulation Geometry	10
2.2 Monte Carlo Algorithm	13
2.3 tMCimg Code	14
2.3.1 Input Files.....	15
2.3.1.1 Segmentation File	15
2.3.1.2 Configuration File.....	16
2.3.2 Output File	17

2.3.2.1 Two Point File	18
2.3.2.2 History File	18
2.4 Data Processing	21
2.4.1 AMIDE Software	21
2.4.2 Least-square Curve Fitting Algorithm	21
3. INSTRUMENTATION AND PHANTOM STUDY	25
3.1 Imaging System	25
3.1.1 Pulsed Laser Source	26
3.1.2 Optical Constant Fraction Discriminator	26
3.1.3 HRI 150/350 PC Interface Card Delay Unit	28
3.1.4 High Rate Control Unit	28
3.1.5 The PicoStar HR ICCD Camera	30
3.1.5.1 Image Intensifier	31
3.1.5.2 CCD Camera	32
3.1.6 High Frequency Laser Synchronization	33
3.2 Phantom Setup	35
3.2.1 Preparation of the Model	35
3.2.2 Data Acquisition in Time Gated Mode	36
4. RESULTS AND DISCUSSION	41
4.1 Monte Carlo Simulation Results	41
4.1.1 Contrast to Background Ratio (CBR).....	41
4.1.2 Full Width at Half Maximum (FWHM).....	48

4.2 Phantom Study Results.....	53
4.2.1 Contrast to Background Ratio and Full Width at Half Maximum.....	53
4.3 Comparison between Experiments and Monte Carlo Simulations.....	59
5. CONCLUSION.....	63
APPENDIX	
A. MATLAB SCRIPTS	65
B. CONFIGURATION FILE	74
REFERENCES.....	76
BIOGRAPHICAL INFORMATION.....	79

LIST OF ILLUSTRATIONS

Figure		Page
1.1	Biliary tree anatomy	1
1.2	Cholecystectomy procedures	4
1.3	Classification of imaging modalities used for biliary tree imaging	5
1.4	Absorption characteristics of tissue chromophores in the near infrared wavelength region.....	9
2.1	(a) Patient based geometry of the biliary tree. The imaging plane intersects the biliary tree at right angles, (b) Simplified tissue geometry for the simulation. Green color circle represents the bile duct.....	10
2.2	3-Dimensional view of tissue geometry implemented for Monte Carlo simulations	11
2.3	Simulation geometry used for reflectance mode (upper figure), simulation geometry used for transmission mode (lower figure)...	12
2.4	Graphical representation of the segmentation file's output.	16
2.5	Steps to read history file as a time series using a Matlab script.....	20
2.6	Schematic showing fitted parameters using a 'Lorentzian Function'	24
2.7	Example of fitted 'Lorentzian Function' at early time gate (left) and at later time gate (right).....	24
3.1	Block diagram of the imaging system	25
3.2	SC-450 pulse laser source.....	26
3.3	Optical constant fraction discriminator unit (left) and internal	

	block diagram of the constant fraction discriminator (right).....	27
3.4	DEL 150/350 delay card.....	28
3.5	Internal block diagram of ICCD camera.....	30
3.6	Internal structure of the intensifier.....	31
3.7	CCD camera	33
3.8	Block diagram of the imaging system	34
3.9	Timing diagram	34
3.10	a) Time gated images for background. b) Time gated images for capillary at 1 mm. c) Time gated images for capillary at 2 mm.....	38
3.11	a) CW background image. b) CW image with capillary at 2 mm depth. c) CW ratio image. d) Intensity profile of the ratio image. e) Fitted lorentzian curve.....	40
4.1	CBR for 0.3 ns gate width in reflectance mode	42
4.2	CBR for 0.3 ns gate width in transmission mode.....	42
4.3	Comparison for maximum CBR between time gated reflectance and time gated transmission mode as a function of the bile duct depth, with 0.03 ns window gate	43
4.4	Comparison for maximum CBR between time gated reflectance and time gated transmission mode as a function of the bile duct depth, with 0.3 ns window gate	43
4.5	Comparison for maximum CBR between CW reflectance and CW transmission mode as a function of the bile duct depth, with 0.03 ns window gate.....	44
4.6	Comparison for maximum CBR between CW reflectance and CW transmission mode as a function of the bile duct depth, with 0.3 ns window gate	45
4.7	Comparison for maximum CBR between time gated reflectance (0.03 ns gate) and time gated transmission mode as a function	

	of the bile duct depth	46
4.8	Comparison for maximum CBR between time gated reflectance (0.3 ns gate) and time gated transmission mode as a function of the bile duct depth	46
4.9	Comparison for maximum CBR between time gated reflectance (0.03 ns gate) and time gated transmission mode as a function of the bile duct depth.....	47
4.10	Comparison for maximum CBR between time gated reflectance (0.3 ns gate) and time gated transmission mode as a function of the bile duct depth.....	47
4.11	Comparison for minimum FWHM between time gated reflectance and time gated transmission mode as a function of the bile duct depth.....	49
4.12	Comparison for minimum FWHM between time gated reflectance and time gated transmission mode as a function of the bile duct depth.....	49
4.13	Comparison for minimum FWHM between CW reflectance and CW transmission mode as a function of the bile duct depth...	50
4.14	Comparison for minimum FWHM between time gated reflectance and time gated transmission mode as a function of the bile duct depth.....	50
4.15	Comparison for minimum FWHM between time gated reflectance mode (0.03 ns gate) and CW reflectance mode as a function of the bile duct depth.....	51
4.16	Comparison for minimum FWHM between time gated reflectance mode (0.3 ns gate) and CW reflectance mode as a function of the bile duct depth.....	52
4.17	Comparison for minimum FWHM between time gated transmission mode (0.03 ns gate) and CW transmission mode as a function of the bile duct depth.....	52
4.18	Comparison for minimum FWHM between time gated transmission mode (0.3 ns gate) and CW transmission mode as a function of the bile duct depth.....	53

4.19	Schematic showing different step size (0.05 ns, 0.1 ns and 0.3 ns) with a fixed gate width of 0.3 ns.....	54
4.20	CBR for 0.3 ns gate width and step size of 0.05 ns.....	55
4.21	CBR for 0.3 ns gate width and step size of 0.1 ns.....	55
4.22	CBR for 0.3 ns gate width and step size of 0.3 ns.....	56
4.23	Comparison of CBR in reflectance mode for absorber at 1 mm, gate width of 0.3 ns and step size of 0.05 ns, 0.1 ns, 0.3 ns.....	56
4.24	Comparison of CBR in reflectance mode for absorber at 3 mm, gate width of 0.3 ns and step size of 0.05 ns, 0.1 ns, 0.3 ns.....	57
4.25	Comparison for maximum CBR for time gated reflectance (gate width 0.3 ns) at different step sizes (0.05 ns, 0.1 ns and 0.3 ns).....	58
4.26	Comparison for FWHM for time gated reflectance (gate width 0.3 ns) at different step sizes (0.05 ns, 0.1 ns and 0.3 ns).....	59
4.27	Comparison for CBR between Monte Carlo Simulations (bile duct at 2 mm) and the phantom experiment (absorber at 2 mm).....	60
4.28	Schematic showing original simulation geometry (left) and modified simulation geometry (right) used to match the experimental data with the simulation data.....	61
4.29	Comparison for CBR for original and modified simulation geometry with a bile duct at 2 mm depth.....	62
4.30	Comparison for CBR for original and modified simulation geometry with a bile duct at 4 mm depth.....	62

LIST OF TABLES

Table		Page
2.1	Ordering of a two-point file. Each block consists of an $N_x \times N_y \times N_z$ block of doubles.....	18
2.2	Format of history file when no detectors are specified. The file contains the (x, y, z, t) position and path length inside each of the n tissue for all N of the exiting photons.....	19
2.3	Format of history file when a non-zero number of detectors are specified. The file contains the number of the detector that recorded the photon and the path length inside each of the n tissue for all N of the exiting photons.....	19

CHAPTER 1

INTRODUCTION

1.1 Biliary Tree and Anatomy

Biliary tree is a path through which bile, a digestive fluid secreted by the liver, is transported to the small intestine. Bile plays an important role in the digestion and the absorption of fat and fat soluble vitamins in small intestine. It is known as tree since it begins with small branches and merges into the common bile duct.

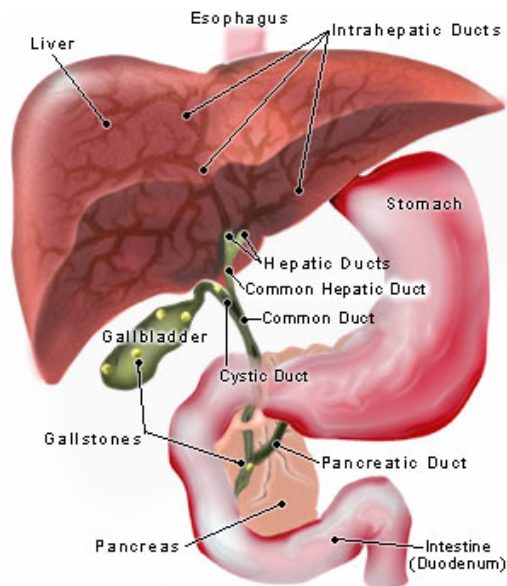


Figure 1.1 Biliary tree anatomy [1].

Figure 1.1 shows the anatomy of the biliary tree which is embedded in fat and other connective tissues [2, 3]. It includes a gallbladder, hepatic ducts, a common hepatic duct, a cystic duct and a common bile duct (CBD). The common hepatic duct is the duct formed by the convergence of right hepatic duct and left hepatic duct. The

common hepatic duct then joins the cystic duct coming from the gall bladder (a small pear shaped organ located beneath the liver on the right side of the abdomen [4] to form the CBD. The CBD varies approximately from 7 - 9 cm in length and after converging with the pancreatic duct it connects into the small intestine.

Major disorders involving biliary tree includes disorders of gallbladder, extrahepatic bile duct and tumors of the gallbladder. However, the most common disorder encountered is cholelithiasis or gallstones.

1.2 Gallstones

Body chemistry, body weight and diet are the major causes of stones formation in the bladder. Gallstones are of two types: cholesterol gallstones and pigment (calcium bilirubin) gallstones [5].

Cholesterol gallstones

In addition to bile, cholesterol is also secreted by the liver. While cholesterol is a fat, bile is a watery solution. In order to dissolve fats in water, liver secretes bile acids and lecithin into the bile. Elevated fat levels and insufficient salts in the bile cause the formation of cholesterol gallstones. Moreover, incomplete and infrequent emptying of bladder causes the bile to over concentrate which in turn gradually transforms bile into stones [6]. Studies suggest that 77 % of the cholelithiasis patients have cholesterol gallstones [7].

Pigment gallstones

Pigment is a waste product formed from hemoglobin, the oxygen-carrying chemical in red blood cells. The hemoglobin from old red blood cells that are being destroyed is changed into a chemical called bilirubin and released into the blood. Thereafter, bilirubin is removed from the blood by the liver. The liver then modifies the bilirubin and secretes the modified bilirubin into bile. The major factor behind the formation of pigment stones is increase in the quantity of the bilirubin which is not only conjugated but also insoluble in the bile. Hence they get accumulated and precipitated forming this type of the gallstones [8].

These stones block the flow of the bile out of the gallbladder and causes cholecystitis or swelling of gallbladder. The only treatment that cures gallbladder disease is a surgical procedure known as cholecystectomy.

1.3 Cholecystectomy

Figure 1.2 shows two ways of performing gallbladder surgery: laparoscopic cholecystectomy and open cholecystectomy. Open cholecystectomy is often performed if complications occur during laparoscopic surgery because of the abnormal anatomy, lack of thrombosis or difficulty in visualizing gallbladder. It is done through a large abdominal incision whereas laparoscopic surgery is done through small punctures in the abdominal wall. Laparoscopic cholecystectomy results in less pain and a faster patient recovery however; it has higher rates of the bile duct injuries as they deprive the surgeon of tactile sensation. Study suggests that occurrence of the bile duct injuries is twice as compared to the open surgeries [9, 10, 11, 12, 13].

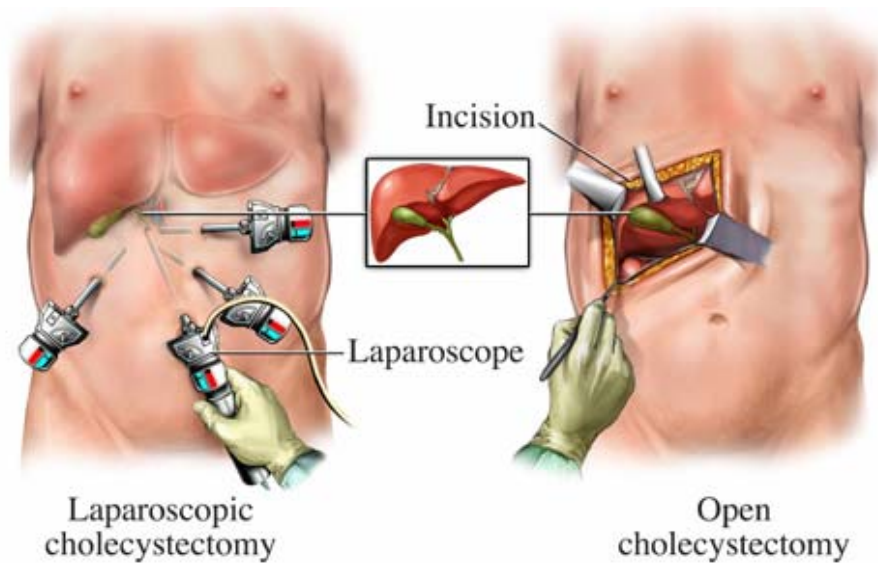


Figure 1.2 Cholecystectomy procedures.

CBD injury during a laparoscopic Cholecystectomy

CBD injury is the most common injury during the laparoscopic Cholecystectomy procedure [14]. An injured bile duct can leak bile which could cause potentially dangerous infection and peritonitis [15]. Approximately, 2000 patients every year suffer from CBD injury in the United States [16]. Many cases of minor injury to the CBD can be managed nonsurgically, while major injury to the bile duct may require corrective surgery. As the biliary tree structures are embedded in fatty tissue, localizing the bile duct is a major challenge for surgeons [17].

In order to reduce the risk of CBD damage various imaging techniques are employed. The following section discusses all current imaging techniques in brief.

1.4 Imaging Modalities

Various imaging modalities have been employed to visualize the biliary tree structures during laparoscopic cholecystectomy. At present, most widely used imaging

modalities are ultrasonography, Magnetic Resonance Imaging (MRI), radiography, nuclear imaging and optical imaging (figure 1.3).

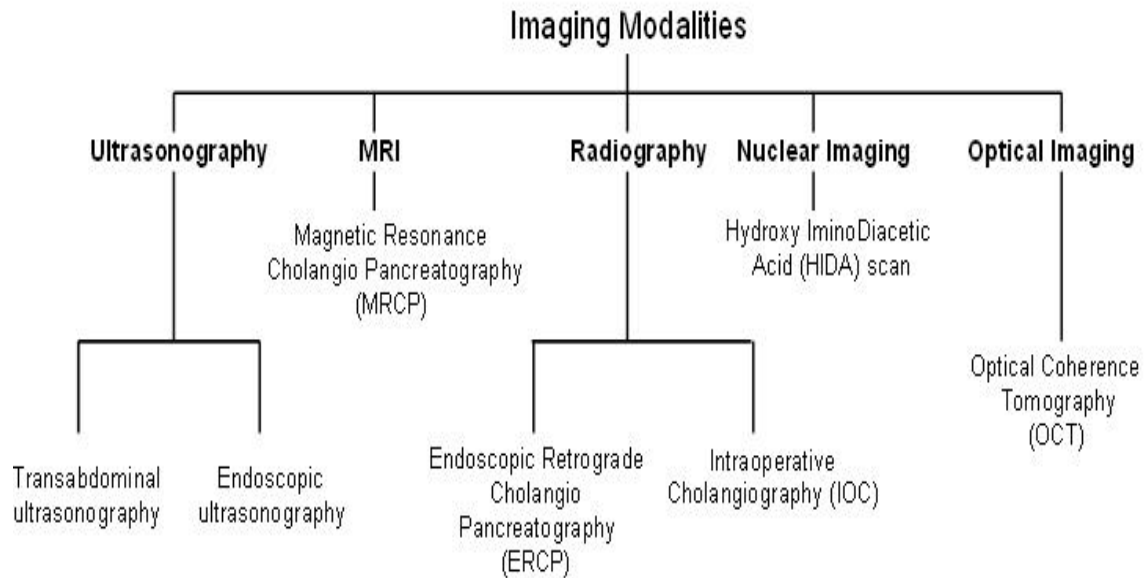


Figure 1.3 Classification of imaging modalities used for biliary tree imaging.

Ultrasonography imaging can be classified as: transabdominal ultrasonography (non-invasive) and endoscopic ultrasonography (invasive). In transabdominal ultrasonography a transducer is placed on the abdomen of the patient and images are captured. The major drawbacks of the system are its poor resolution, contrast and inability to see object smaller than 4-5 mm. In endoscopic ultrasonography system a transducer is placed at the end of an endoscope and inserted into the intestinal tract. As the transducer is in close proximity of the imaging object, it allows high resolution imaging of the biliary structures [18]. However, endoscopic ultrasonography is expensive and could cause intravenous sedation and intestinal perforation.

Magnetic Resonance Cholangio Pancreatography (MRCP) scan is a modified MRI protocol to image bile and pancreatic ducts. As MRI separates tissues and organs based on their water concentration, MRCP provides high resolution imaging of the bile within the gallbladder and the bile ducts. Moreover, it can also detect bile leaks and obstruction of the ducts. This technique is non invasive and does not use radiation for imaging. However, slower image acquisition rate as compared to CT scan, breath hold during the scan and cost prevents MRCP to become a popular imaging technique.

Radiographic procedure includes: Endoscopic Retrograde Cholangio Pancreatography (ERCP) and Intra-Operative Cholangiography (IOC). ERCP is an x-ray procedure to examine duodenum, papilla, bile ducts, gallbladder and pancreatic duct. Following sedation, a duodenoscope is passed into the duodenum for imaging papilla (a small nipple like structure where the common bile and pancreatic duct enter duodenum). Thereafter, contrast material (dye) is injected through a plastic catheter into the papilla. The major advantage of ERCP lies in its ability as a diagnostic as well as therapeutic tool. However, perforation of the duodenum by the duodenoscope and pancreatitis are the two major risks involved with this imaging modality [19].

IOC is performed by injecting a contrast agent in the cystic duct and obtaining radiographic images. IOC provides a surgical road map of the CBD [20]. Thus the IOC might decrease the rate of the bile duct injuries but cannot fully prevent them as this technique has its own limitations. In order to perform IOC, catheterization of the cystic duct is necessary. However, this invasive procedure tends to cause injuries and might lead to severe inflammation [21]. It has also been demonstrated that IOC is

costly and time inefficient in preventing the bile duct injuries and therefore is not widely practiced during cholecystectomy procedures [22].

Hydroxy Iminodiacetic Acid (HIDA) scan is an invasive nuclear imaging technique to image obstructions of the bile ducts and the bile leaks. A radioactive tracer is injected intravenously and absorbed by the liver and excreted into the bile ducts. Thereafter, a special scanner is placed over the patient's abdomen and path of the radioactive chemical is traced throughout the biliary tract [19].

Optical coherence tomography (OCT) is an optical imaging modality introduced in 1991 [23] that performs high-resolution, cross-sectional, subsurface tomographic imaging of the internal microstructure in materials and biological systems by measuring backscattered or back reflected infrared (IR) light. The physical principle of OCT is similar to that of B-mode ultrasound imaging, except that the intensity of infrared light is measured rather than that of the sound waves [24]. The OCT imaging from the GI tract can be done in humans by using narrow-diameter, catheter-based probes [25]. The probe is inserted through the accessory channel of a side-view endoscope inside a standard transparent ERCP catheter for investigating the biliary tree. Wavelengths of the infrared light used in OCT are one to two orders of magnitude higher than ultrasound wavelength, so OCT technology can yield a lateral and axial spatial resolution of about 10 micron, which is 10-25 fold better than that of available high-frequency ultrasound imaging. However, superficial imaging depths make the OCT a less useful imaging technology for biliary tree imaging [26].

1.5 Motivation for Research

As currently available imaging modalities have drawbacks, there is a growing demand to develop a safe, cost and time effective non-invasive imaging technique which could assist surgeons during the laparoscopic cholecystectomy. In the past few years near infrared (NIR) spectroscopy has emerged as a potential imaging technique for biliary tree imaging. Light incident on tissue undergoes multiple scattering and absorption. Figure 1.4 shows the absorption spectra of various chromophores in the tissue in NIR wavelength range (700-900 nm). NIR photons are absorbed less by the tissue chromophores as compared to visible photons [27], which in turn results in greater penetration in tissue by the NIR photons. Light propagation in the tissue is dependent on the absorption and scattering phenomenon; which are tissue specific and thus enable us to study the unique optical features of different tissues [28]. These properties make NIR spectroscopy a useful tool to image biliary tree structures. This technique can be used to differentiate tissues based on their optical properties; however, depth resolved imaging using NIR spectroscopy in continuous wave (CW) mode is not possible.

To overcome this limitation of NIR spectroscopy, a time resolved optical imaging technique to resolved tissues and organs at different depths is proposed. The purpose of this work is to show that the proposed time resolved optical imaging technique has an edge over continuous wave (CW) system in terms of contrast and resolution in visualizing biliary tree structures embedded within fatty tissue.

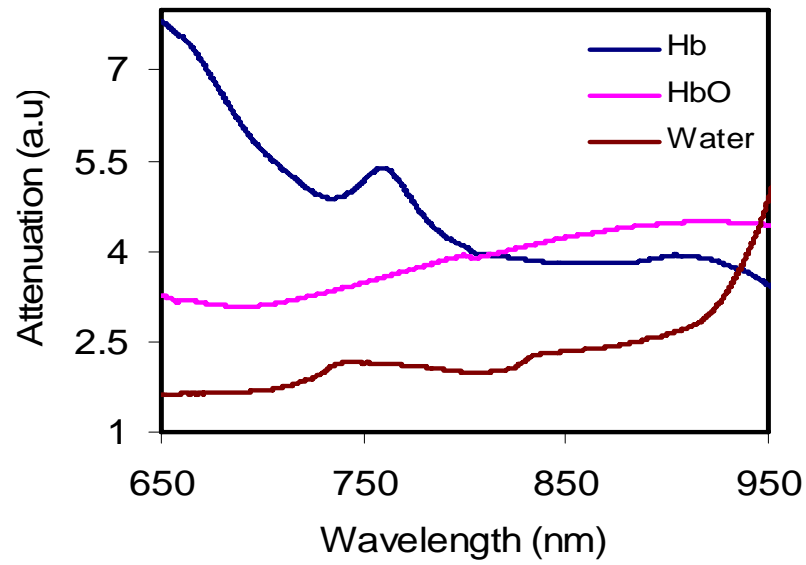


Figure 1.4 Absorption characteristics of tissue chromophores in the near infrared wavelength region.

CHAPTER 2

MONTE CARLO SIMULATIONS

2.1 Simulation Geometry

The biliary tree structure consists of the bile duct with the hepatic artery and portal vein running along it [3]. These structures are embedded into connective tissue and fat at a depth of 2-6 mm from the fatty tissue surface and therefore cannot be directly visualized by the surgeon. Clinical experiment has shown that there can be significant variation in anatomical geometry and spatial orientation of biliary tree structures between patients.

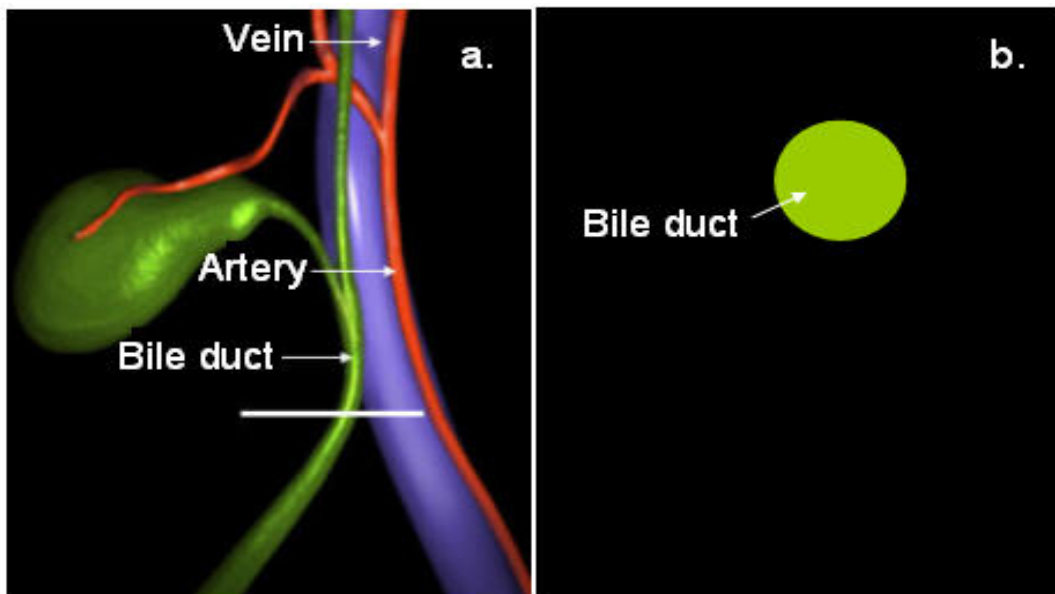


Figure 2.1 (a) Patient based geometry of the biliary tree. The imaging plane intersects the biliary tree at right angles, (b) Simplified tissue geometry for the simulation. Green color circle represents the bile duct.

For the feasibility study of the time resolved imaging system, we have considered just the CBD. It was simulated as a cylinder running parallel to the surface of the fat layer. The CBD will be henceforth referred to as the ‘bile duct’. The imaging plane intersects this parallel cylinder at the right angle making it appear as circle at a face-on view of the intersection plane (figure 2.1).

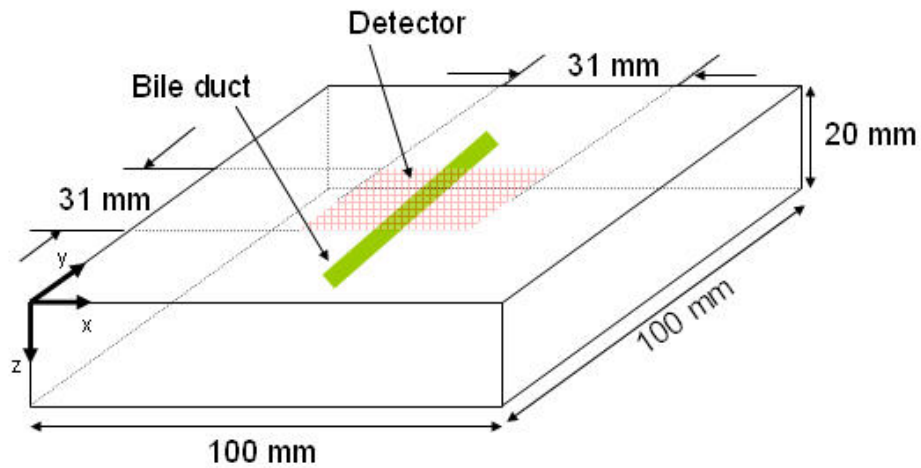


Figure 2.2 3-Dimensional view of tissue geometry implemented for Monte Carlo simulations.

Figure 2.2 shows 3-Dimensional (3D) simulation geometry, while figure 2.3 shows simulation geometry used for reflectance and transmission mode respectively. Within a 3D volume (100 X 100 X 20 mm) of adipose tissue a 4 mm diameter bile duct was kept. Moreover, to simulate the Field Of View (FOV) of the ICCD camera, a 31 X 31 mm region was assigned as detectors. Furthermore, planar illumination pattern was implemented for both transmission and reflectance mode. In order to accommodate fat layer thickness variations, bile duct was initially kept at 2 mm from the surface of fat

and then it was moved by one mm until 14 mm. Simulations were repeated for transmission as well as reflectance mode.

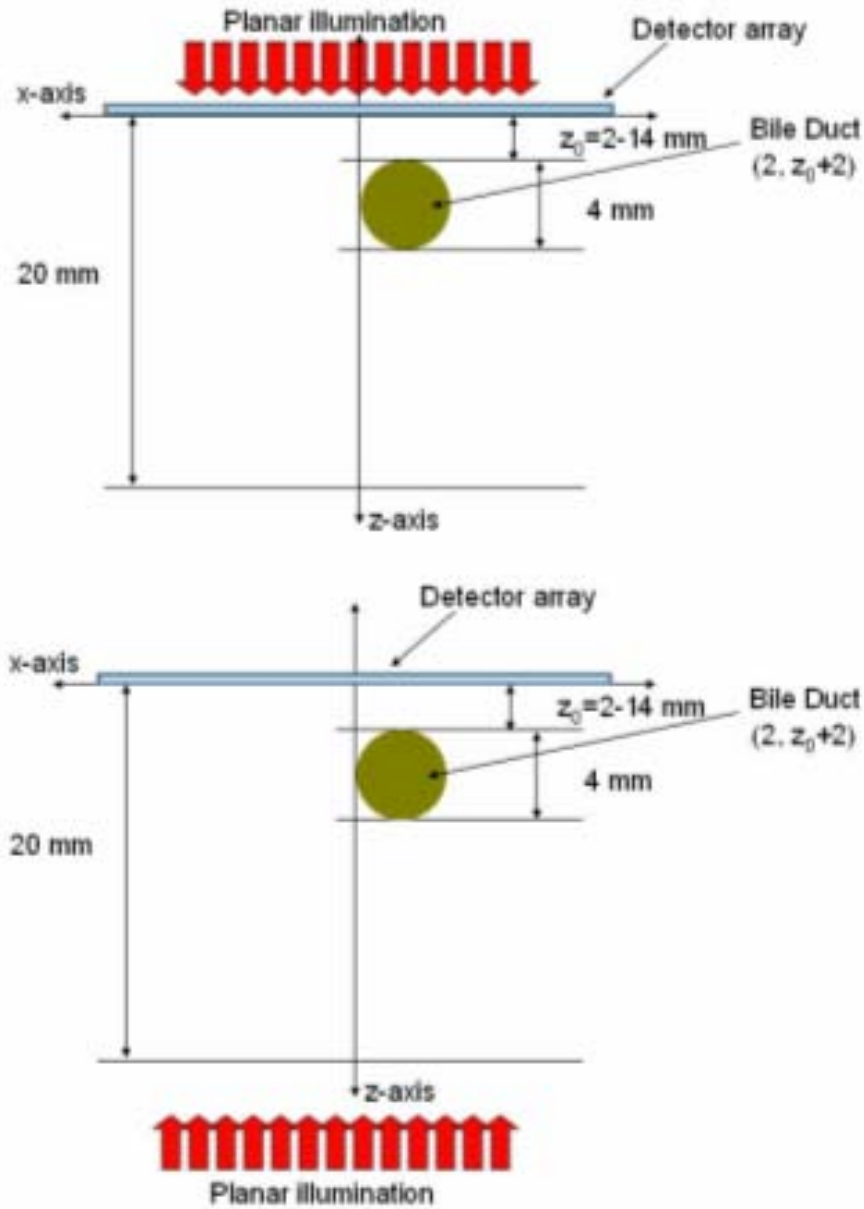


Figure 2.3 Simulation geometry used for reflectance mode (upper figure), simulation geometry used for transmission mode (lower figure).

2.2 Monte Carlo Algorithm

Monte Carlo Simulations for light transport is a stochastic method to model photon propagation in tissues. Theoretically, it can simulate the physical process of photon transport without making any approximations. However, in reality Monte Carlo codes often simulate approximate transport models because the details of the photon-tissue interaction processes are too complicated. Approximations are also often made to reduce computation time.

At the beginning of each simulation, finite numbers of photons are launched into the tissue with a predefined direction and position. Thereafter, photons of a defined light wavelength are propagated through the predefined tissue volume geometry that has been assigned appropriate optical properties for each tissue type and photon wavelength. As a photon propagates from one scattering event to next, a check is made on each grid spacing to see if the scattering coefficient (μ_s) or absorption coefficient (μ_a) has changed. If the scattering coefficient has changed, the remainder scattering length is normalized ($\mu_s^{\text{old}}/\mu_s^{\text{new}}$). Moreover, if the μ_a has changed, the photon weight is decreased with the new absorption coefficient [29]. The step length choice is based on a negative exponential probability function and the new scatter direction is based on the Henyey-Greenstein phase function [30].

Photons are propagated until they reach an air-tissue boundary, whereupon a decision is made on whether they will be totally reflected and continue to propagate in tissue or exit into air. To reduce computation time, if a photon is trapped in tissue for a time that is much longer (10 ns) than typical tissue escape times (1 ns), the simulations

gives up on that photon and starts a new photon history [31]. However, if the photon exits in a location that has been predefined as a detector location, then information is recorded in a history file identifying the detector and path length of the photon in each tissue type prior to being detected [31].

2.3 tMCimg Code

In this study, I used tMCimg code which uses a Monte Carlo algorithm to model the transport of photons through 3D volumes with spatially varying properties and arbitrary boundary condition. The tMCimg code simulates the transport of photons through bile duct geometry described in figure 2.1 and score photons in a 2D array of matrix (figure 2.2). The code was downloaded from the photon migration imaging lab at MGH/MIT/HMS Athinoula A. Martinos Center for Biomedical Imaging website.

For every photon in the simulation following steps were performed:

1. The initial position and direction was set for source as well as detector according to the configuration file
2. Until the photon escaped:
 - (a) The distance to the next scattering event was set. This is an exponentially distributed random variable.
 - (b) Photon was moved, possibly reflecting or refracting off of interfaces, to the next scattering event. As the photon is moved from voxel to voxel, it is attenuated according to the local absorption.
 - (c) The contribution of this photon's path was then added to the accumulated photon fluence.

(d) Photon was scattered into a new direction according to some (possibly isotropic) phase function.

(e) Iteration was done until the photon leaves the system, or the time limit is exceeded.

3. Finally, it was saved to disk.

2.3.1 Input Files

Two files control the behavior of the tMCimg code which includes the segmentation file and the configuration file. The segmentation file is a mapping between voxels and tissue types and thus, indirectly maps the voxels and the optical properties. The configuration (input) file defines the optical properties and simulation parameters.

2.3.1.1 Segmentation File

The segmentation file is a continuous block of data in which one unsigned 8-bit number is assigned for every voxel being modeled. Matlab (a commercial software package, The Mathworks Incorporated, Natick, Massachusetts) script for generating voxelized model is shown in Appendix A. To match the proposed simulation geometry (section 2.1), first a 100 X 100 X 20 mm 3D volume was created. Thereafter, value '0' was assigned to the outermost layer to define it as "air"; any photon making its way into the air was assumed to have left the system. A photon was recorded by a given detector if it exit into "air" and its final position was within the specified radius of the detector location. Further, value '1' was assigned to define adipose tissue and '2' was used to

define bile duct within the volume. Figure 2.4 shows the graphical representation of output of the segmentation file which was then fed to the configuration file.

2.3.1.2 Configuration File

Configuration file is an input file for the tMCimg code. It provides source-detector position, orientation and dimensions. Moreover, it is used to pass optical properties for different tissue types, number of photons, number of time gates and gate width to be simulated.

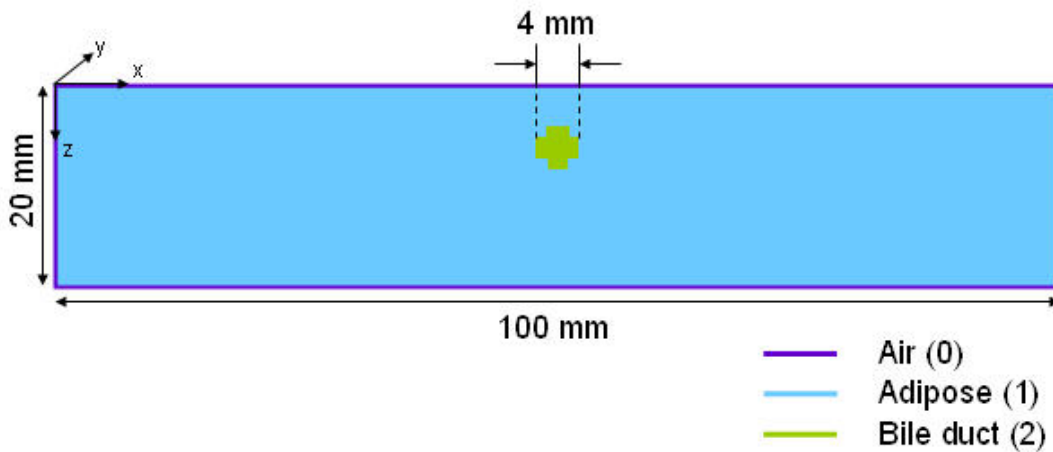


Figure 2.4 Graphical representation of the segmentation file's output.

Appendix B shows a configuration file used for this study. Simulations were performed using 150 million photons, 50 time gates with a gate width of 0.03 and 0.3 ns. Moreover, keywords “Source” and “Detector” were used to introduce source-detector definitions respectively. Each definition was surrounded by curly brackets ‘{}’. Further, “pos” (position), “rad” (radius), “dir” (direction) and “na” (numerical aperture) were the parameters passed within the definition. However, “dir” and “na” are optional parameters and for this study default value (zero) for “na” was used. To

match the simulation geometry in reflection mode as well as in transmission mode, 0.5 mm detector radius and 45 mm source radius were chosen. Moreover, in reflection mode source position was kept in the positive z direction ($z = 1$ in Appendix B) and in transmission mode it was kept in the negative z direction ($z = -1$ in Appendix B). A 31 X 31 2-Dimensional (2D) detector array was defined in the top layer of the volume to define the field of view of the system.

Further, tissue types were specified as input to the Monte Carlo code and referred to voxel groups with identical optical properties. The tMCimg supports up to 100 different tissue types [31]. Keyword “Tissue” was used to introduce a set of tissue optical properties. For every “Tissue” declaration in segmentation file, absorption coefficient ($\mu_a = 0.3 \text{ mm}^{-1}$ and 0.00519 mm^{-1} for bile and adipose respectively), reduced scattering coefficient ($\mu_s' = 0.625 \text{ mm}^{-1}$ and 1.133 mm^{-1} for bile and adipose respectively), scattering anisotropy ($g = 0.01$) and index of refraction ($n = 1.4$) were defined. Further, “nxvoxel”, “nyvoxel” and “nzvoxel” which specify the number of voxel in each (x, y, z) dimension were selected as 100, 100 and 20 respectively. Moreover, a default value of $2.99792458 \times 10^{11} \text{ mm/s}$ was used for the speed of light. This in turn, did set the fundamental length scale of the program to be millimeters. Furthermore, “dx”, “dy” and “dz” defined the size of the voxels. Currently only cubic voxels are supported by the code. For this study 1 mm voxel size was set.

2.3.2 Output File

Output of the tMCimg consists of two data files: the history file (*.his) and the two point file (*.2pt). They are described briefly in the following sections.

2.3.2.1 Two Point File

The two-point file (*.2pt) contains the photon density at every voxel and time gate, as computed by the Monte Carlo simulation. Moreover, it stores data as “double” and the voxels are ordered the same way as the segmentation file. Further, the real part of all the time gates are written out sequentially, followed by the imaginary parts. Table 2.1 depicts the ordering of the two-point file.

Table 2.1 Ordering of a two-point file. Each block consists of an $N_x \times N_y \times N_z$ block of doubles

Time Gate 1 Real Part	Time Gate 2 Real Part	..	Time Gate N Real Part
⋮			
Time Gate 1 Imaginary Part	Time Gate 2 Imaginary Part	..	Time Gate N Imaginary Part

2.3.2.2 History File

The history file (*.his) contains a record of every photon that successfully traverses the volume. Based on the settings in the configuration file, there are two different file formats for the history file. If no detector is specified, then the (x, y, z) location of every photon exiting the medium is recorded together with the time and the distance the photon traveled inside each tissue type (Table 2.2). If at least one detector is specified, the number of the detector that saw the photon is recorded, along with the time and lengths as before (Table 2.3).

In order to analyze simulation results, the history file was read through a Matlab script (Appendix A). The history file contains the number of detector that records the

photon and the path length inside each of the n tissues for all of the exiting photons as a 32-bit floating point number. In this study, photon history was gathered for 961 detector, 50 time gates and 2 tissue types in a format shown in Table 2.3.

Table 2.2 Format of history file when no detectors are specified. The file contains the (x, y, z, t) position and path length inside each of the n tissue for all N of the exiting photons.

x_1	y_1	z_1	t_1	$l_1^{(0)}$	$l_1^{(1)}$	$l_1^{(n)}$
x_2	y_2	z_2	t_2	$l_2^{(0)}$	$l_2^{(1)}$	$l_2^{(n)}$
⋮							
x_N	y_N	z_N	t_N	$l_N^{(0)}$	$l_N^{(1)}$	$l_N^{(n)}$

Table 2.3 Format of history file when a non-zero number of detectors are specified. The file contains the number of the detector that recorded the photon and the path length inside each of the n tissue for all N of the exiting photons.

d_1	t_1	$l_1^{(0)}$	$l_1^{(1)}$	$l_1^{(n)}$
d_2	t_2	$l_2^{(0)}$	$l_2^{(1)}$	$l_2^{(n)}$
⋮					
d_N	t_N	$l_N^{(0)}$	$l_N^{(1)}$	$l_N^{(n)}$

A Matlab script read the history file in a segment of 4. First two elements of each segment give the detector and time gate numbers, respectively. While last two gives the photon pathlength in adipose tissue and bile duct, respectively. Pathlength in each tissue type was scaled by their respective μ_a values and added together to get an attenuated intensity for each traversed photon within the volume. These values were first stored as 961 X 50 2D matrices as shown in figure 2.5, where 961 indicate total number (31 X 31) of detector used for the simulations and 50 indicates total number of

gates. Further, this 2D matrix was decomposed into 31 X 31 X 50 3D matrices (figure 2.5), in which each 31 X 31 2D matrices represents a time gate. For further analysis, this 3D matrix was stored in a binary file and analyzed by AMIDE software.

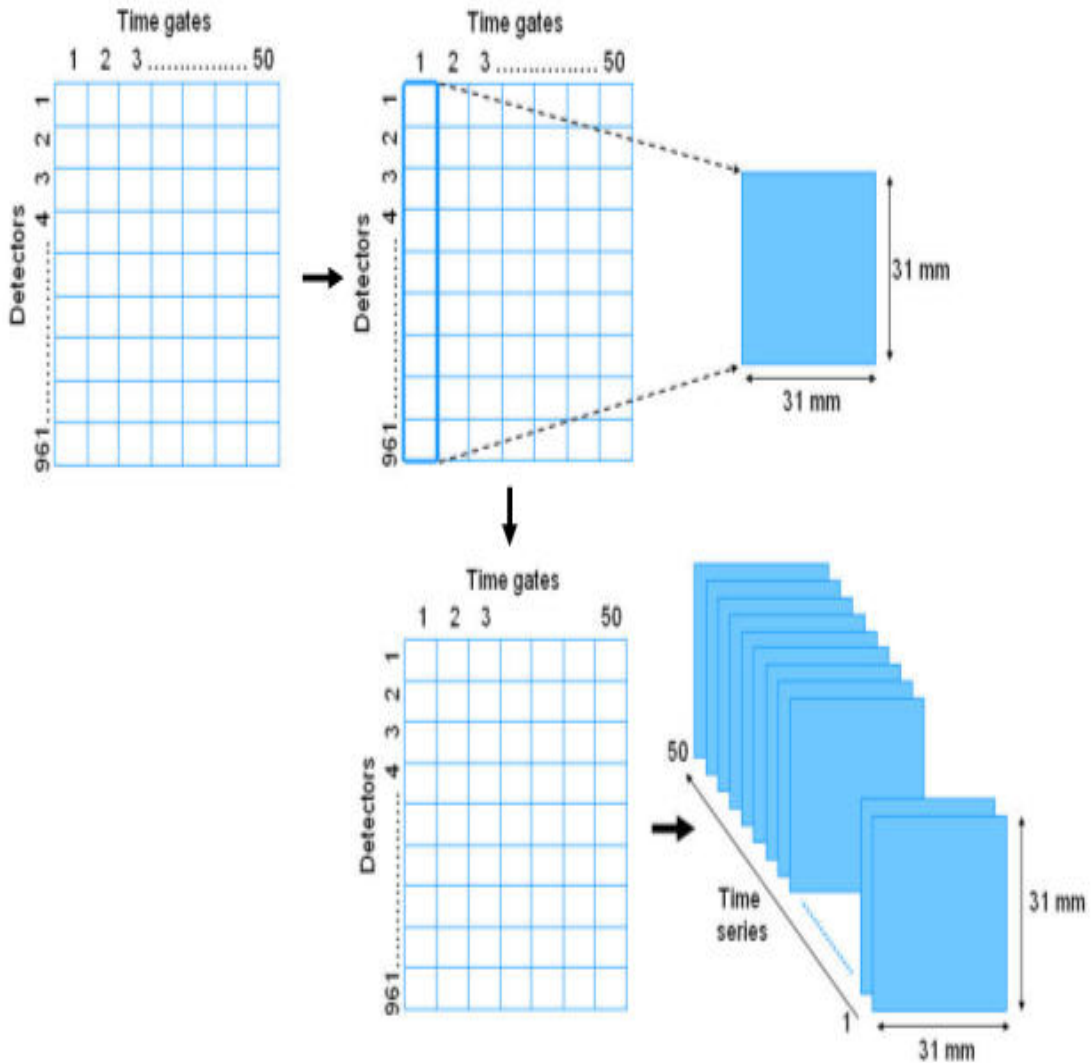


Figure 2.5 Steps to read history file as a time series using a Matlab script.

2.4 Data Processing

2.4.1 AMIDE Software

AMIDE (Amide's Medical Image Data Examiner) is an open source tool developed for the purpose of viewing and registering medical images. It is capable of performing 3D quantitative analysis of microPET data. Moreover, it is used for registering microPET and microCT data sets [32]. Here, we are using it for reading 3D time gated binary data set.

Initially, a *.bin file (2 mm depth) was read into AMIDE using double, little Endian (64 bit) format. In order to match the dimensions of the *.bin file, the values of x, y, z were chosen as 31, 31, 50 respectively. Additionally, the voxel size was chosen as 1 mm³ in AMIDE. Thereafter, the data set was filtered using a median 3D filter. We used median 3D filter as it prevents edges and removes speckle noise. Once filtered, the data set was read slice by slice for all 50 gates and line profiles for each gate were stored into text files. The above procedure was repeated for depths from 3 - 14 mm.

2.4.2 Least-Square Curve Fitting Algorithm

In order to analyze change in resolution and contrast as a function of depth, these individual intensity profiles were analyzed for their shape and were fitted with a 'Lorentzian Function' (equation 1) for all time gates.

$$f(x) = a - \left[\left(\frac{1}{2\pi} \right) \left(\frac{d}{(x-c)^2 + \left(\frac{d}{2} \right)^2} \right) \right] \dots \dots \dots (1)$$

Where, ‘a’ represents background, ‘c’ represents the center and ‘d’ controls the width and amplitude of the lorentzian curve. In order to quantify the change in amplitude with respect to change in depths, an additional term ‘b’ was introduced in equation 1.

$$f(x) = a - \left[\left(\frac{b}{2\pi} \right) \left(\frac{d}{(x-c)^2 + \left(\frac{d}{2} \right)^2} \right) \right] \dots \dots \dots (2)$$

In equation 2, combined value of ‘b’ and ‘d’ represents amplitude, ‘c’ represents position of the peak (center) and ‘d’ represents width of the curve. The curve fitting was implemented using the ‘fit’ function in Matlab. This function solves non-linear least square problems. The input parameters to be specified for this function were the column vector of predictor data, column vector of measured data (intensity), the starting estimates of all four parameters (a, b, c, d) and the lower and upper bounds within which the solution set of the parameter should lie. These upper and lower bound were specified based on existing values [33]. The algorithm found a fit where the least square error between the measured and the fitted data was minimum for a default number of iterations. Moreover, confidence interval for each fitted parameter was computed using the ‘confint’ function in Matlab. Finally, for the purpose of data analysis, two terms ‘contrast to background ratio’ and ‘FWHM’ were defined from the fitted parameters. Figure 2.6 shows the graphical representation of the fitted parameters. For this study contrast was defined as

$$contrast = \left(\frac{2b}{\pi d} \right) \dots\dots\dots (3)$$

While the value of ‘d’ represents the FWHM of the fitted curve.

Furthermore, error for ‘FWHM’ was computed using the equation 6. As contrast is ‘b’ and ‘d’ dependent term, its error could not be computed by a simple multiplication between the errors for ‘b’ and ‘d’. Hence, error propagation for contrast was found out using the equation 7. Moreover, error for ‘contrast to background ratio’ was calculated using equation 8. Figure 2.7 shows the fitted ‘Lorentzian Function’ for an early and later time gates.

$$Error\ in\ background = fitted\ (a) - lower\ confidence\ limit\ (a) \dots\dots\dots (4)$$

$$Error\ in\ b = fitted\ (b) - lower\ confidence\ limit\ (b) \dots\dots\dots (5)$$

$$Error\ in\ FWHM = fitted\ (d) - lower\ confidence\ limit\ (d) \dots\dots\dots (6)$$

$$Error\ in\ contrast = contrast \times \sqrt{\left(\left(\frac{error(b)}{fitted(b)} \right)^2 + \left(\frac{error(d)}{fitted(d)} \right)^2 \right)} \dots\dots\dots (7)$$

Error in contrast/background =

$$contrast/background \times \sqrt{\left(\left(\frac{error(background)}{fitted(background)} \right)^2 + \left(\frac{error(contrast)}{fitted(contrast)} \right)^2 \right)} \dots\dots\dots (8)$$

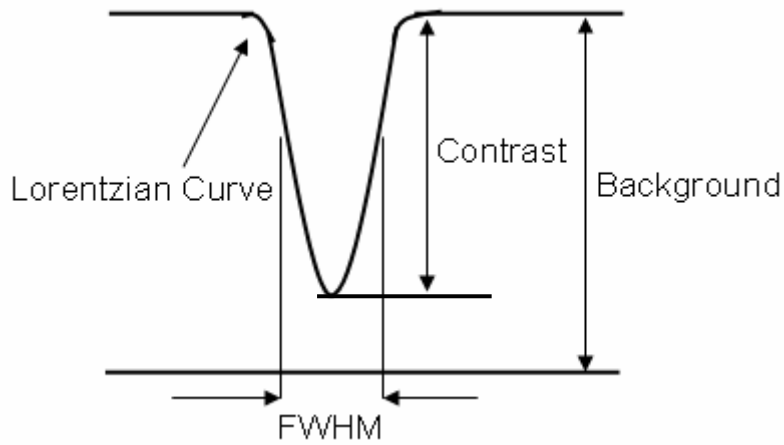


Figure 2.6 Schematic showing fitted parameters using a 'Lorentzian Function'.

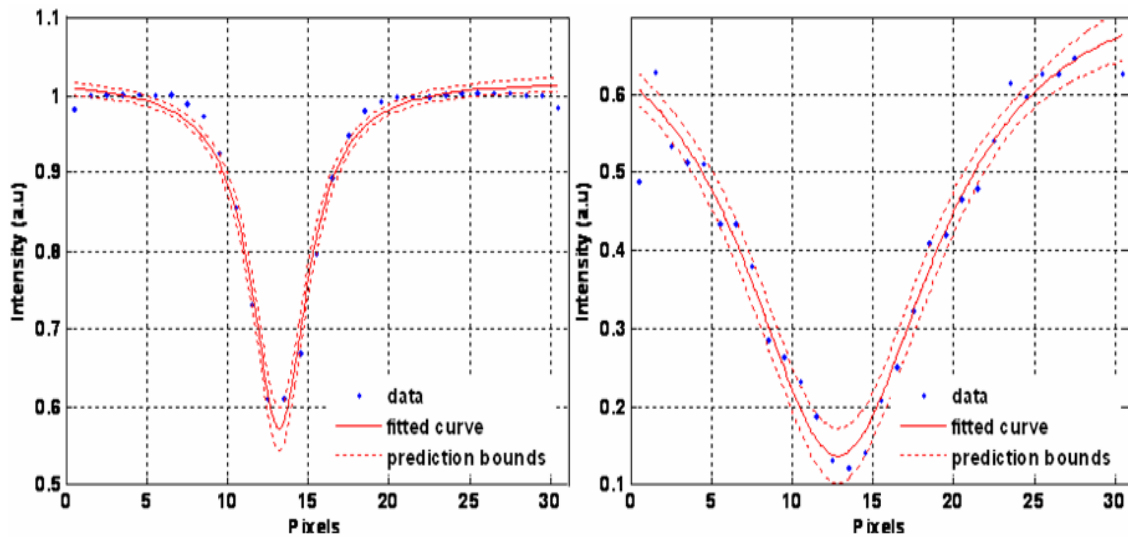


Figure 2.7 Example of fitted 'Lorentzian Function' at early time gate (left) and at later time gate (right).

CHAPTER 3

INSTRUMENTATION AND PHANTOM STUDY

3.1 Imaging System

Figure 3.1 shows the block diagram of the time resolved optical imaging system (LaVision Inc.) employed for the phantom study. It has a pulsed laser, a constant fraction discriminator (CFD), a High Rate Imager (HRI) control unit, a PC based delay unit and an ICCD camera. The system uses a Cooke SensiCamQE CCD camera coupled with a gated image intensifier (LaVision PicoStar HR, LaVision GmbH, Göttingen, Germany) for light detection. The HRI control unit (Kentech Instruments Limited, Oxfordshire, England) and a picosecond delay unit (Kentech) allow the acquisition of images with gate widths of 200 ps with a temporal step size of 25 ps. Following sections explain the system components in detail.

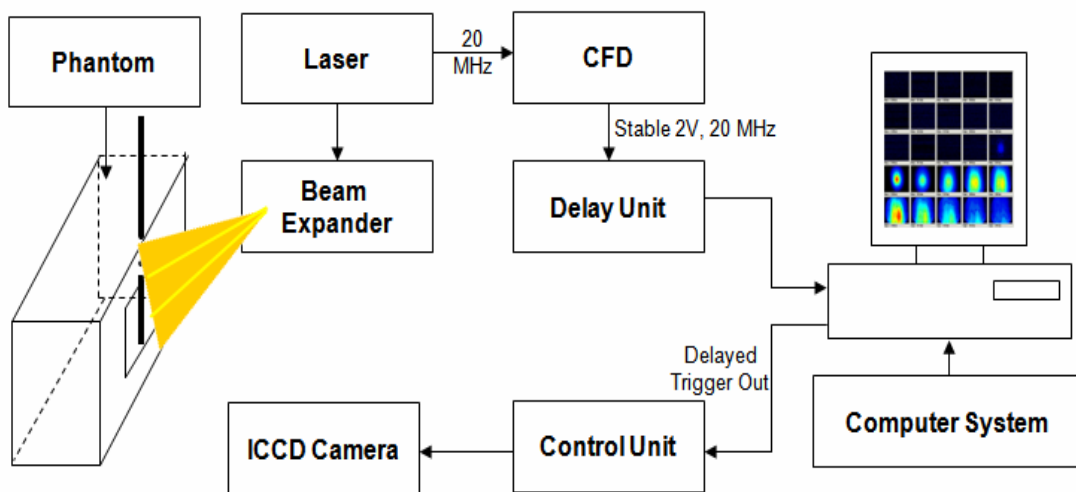


Figure 3.1 Block diagram of the imaging system.

3.1.1 Pulsed Laser Source

Figure 3.2 shows a SC-450 ultra fast laser (Fianium Inc.), which was used as a source of illumination as well as a trigger for the delay generator. It is a class 4, 450-1800 nm broadband pulsed source with a central wavelength of 1064 nm. Moreover, it has a repetition rate of 20 MHz and an average power of 2 W. As there are no safety glasses covering entire spectral range of this laser, all the initial alignments were performed at 10-20 % of the full power to prevent any injury to the eye.



Figure 3.2 SC-450 pulse laser source.

3.1.2 Optical Constant Fraction Discriminator

The Optical Constant Fraction discriminator (OCFD) is designed to obtain stable electrical pulses when triggered by unstable electrical/optical pulse. The OCF-400 (figure 3.3) was used to trigger the delay unit with stable pulses regardless of the unstable amplitude from the laser.

Figure 3.3 (right) depicts the basic block diagram of the OCFD. Input to the OCFD can be optical or electrical trigger signal. In case of optical laser pulses, a fast

PIN photo diode detects the optical pulse and converts it to electrical pulse. However, in this study we used the electrical signal (trigger out from the laser) as an input signal for the OCFD. The electrical pulse is simultaneously fed to a leading edge discriminator and a zero cross discriminator. The zero cross discriminator is a differential comparator that gets the photo diode pulse at both input terminals. The pulse at the -ve input was delayed by a fraction of the pulse width which helps the comparator to see a bipolar pulse effectively. Ideally, the zero cross point of this pulse does not depend on the pulse amplitude. The negative transition of the zero cross discriminator indicates the temporal position of the optical pulse. To obtain a defined trigger threshold, a leading edge discriminator has been used in parallel with the zero discriminator. The leading edge discriminator responds when the pulse exceeds an adjustable threshold value. The output pulse of the leading edge discriminator is used to enable the output pulse stage of the OCF-400. As a result, the OCF-400 delivers a stable 2V output pulse only for input pulses above a selectable energy. This signal was then used to trigger the delay unit.

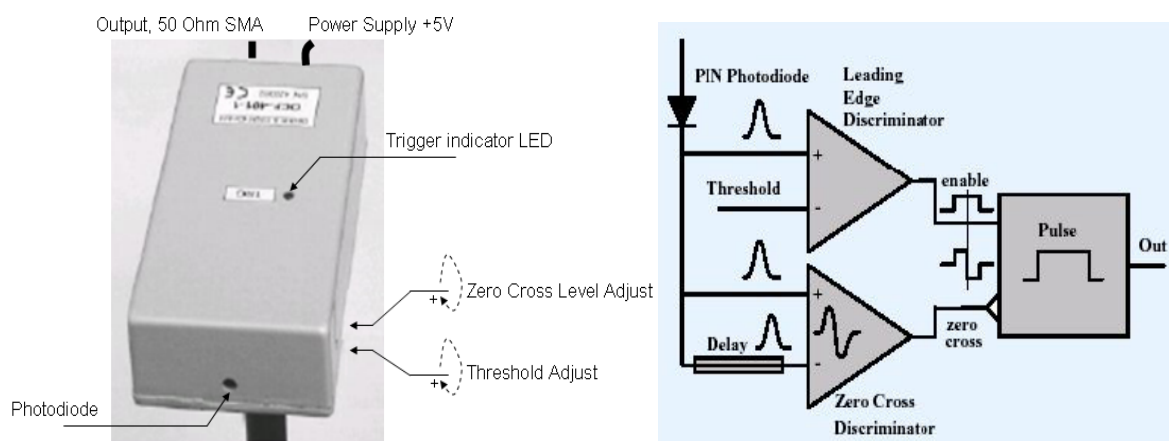


Figure 3.3 Optical constant fraction discriminator unit (left) and internal block diagram of the constant fraction discriminator (right).

3.1.3 HRI 150/350 PC Interface Card Delay Unit

The PicoStar camera system provides three different delay units that is a ps-delay unit, a DEL 150/350 PC interface card and a HRI delay unit for high resolution time delay control. However, for the purpose of this study a DEL 150/350 PC interface card (figure 3.4) was used as a delay generator.

The DEL 150/350 interface card is a device which provides delays with ps resolution. It delays the external triggers (output from the OCF) with a programmable gate length. When an external trigger is received, the programmed delay time and the gate width are processed with an internal propagation delay time of 10 ns. Moreover, any additional trigger during this processing time is ignored which results in a maximum repetition rate of 20 MHz (DEL 150) and 30 MHz (DEL 350) for small delays and gate widths.



Figure 3.4 DEL 150/350 delay card.

3.1.4 High Rate Control Unit

The main function of the High Rate control unit is to gate the intensifier and provide gain modulation by switching photo cathode potential with respect to the MCP input. The principle of fast gating is that the tube is biased off by means of a small positive potential applied to the cathode with respect to the MCP input. In order to gate

the camera on, a short duration negative pulse is applied to the relatively high capacitance load presented by the cathode via a low impedance matching network.

The HRI controller unit, which drives the image intensifier head, has four sections:

1. Low voltage board:

The low voltage board provides power to all sections within the intensifier. It also includes a 24 V supply and a switchable 54V amplifier supply. Logic voltages (ECL and TTL) are also generated on this board.

2. High voltage tube bias supply:

The high voltage tube bias supply provides the static potentials required for the intensifier tube. Moreover, it contains several programmable regulators driven from a common oscillator.

3. Signal conditioning section:

This section provides mode selection (RF, COMB, logic, inhibit), trigger selection (+ve or -ve edge triggering, level triggering), threshold termination and trigger selection, COMB impulse generation, RF gain control, logic selection (TTL or ECL) and TTL monitor output.

4. Internal computer control:

The HRI is controlled by a TDS2020 microcontroller, Hitachi H8 microprocessor. The card contains 6, 12 bit D-A converters which control the pulser, power supply and signal conditioning cards. In addition the microprocessor monitors the push buttons, tube temperature, phosphor current and power supply load.

3.1.5 The PicoStar HR ICCD Camera

A PicoStar ICCD camera was used as a light detector in this study. The major component of the camera consists of an intensifier including a control unit. This system is developed and built by “Kentech Instruments Ltd.”, which uses specially designed image intensifiers from company “PHOTONIS”.

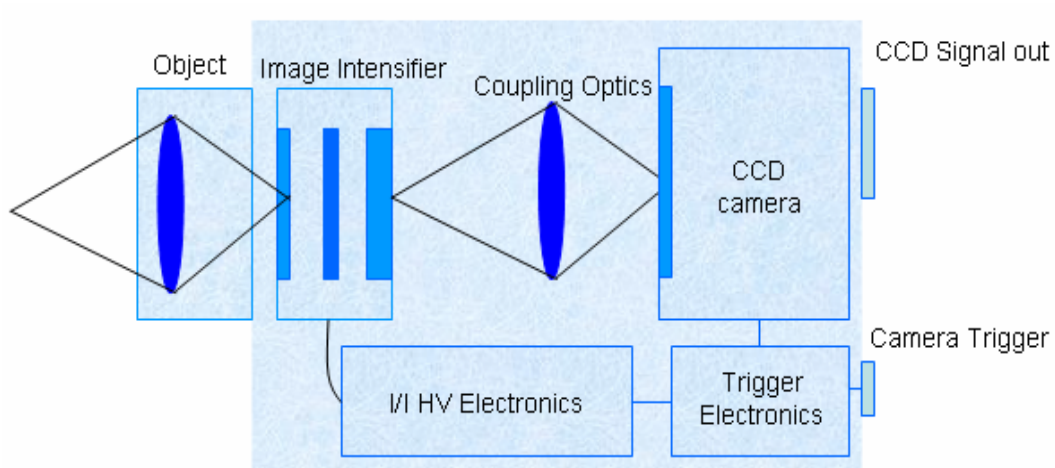


Figure 3.5 Internal block diagram of ICCD camera.

Figure 3.5 shows the internal block diagram of the ICCD camera. An ICCD camera consists mainly of two devices that co-operate exactly to capture the desired information. These are: the CCD camera and the image intensifier. The purpose of using an intensifier is to provide an electronic shutter which can open in nanosecond range. The light is focused to the image intensifier entrance window, which is then converted to electrons and amplified within the intensifier. Thereafter, electrons are converted back to light photons and recovered at the exit window at image intensifier. Further, the image at the exit window is focused onto the CCD chip by lens coupling.

3.1.5.1 Image Intensifier

Figure 3.6 shows a cross sectional view of a single stage proximity focused image intensifier. Intensifier is placed in front of the CCD camera through lens. It is gateable and acts as a fast shutter. It contains three main components: A photo cathode, a micro channel plate (MCP) and a phosphor screen (Figure 3.6 - right) enclosed within a cylindrical ceramic housing with suitable leads for electrical connection.

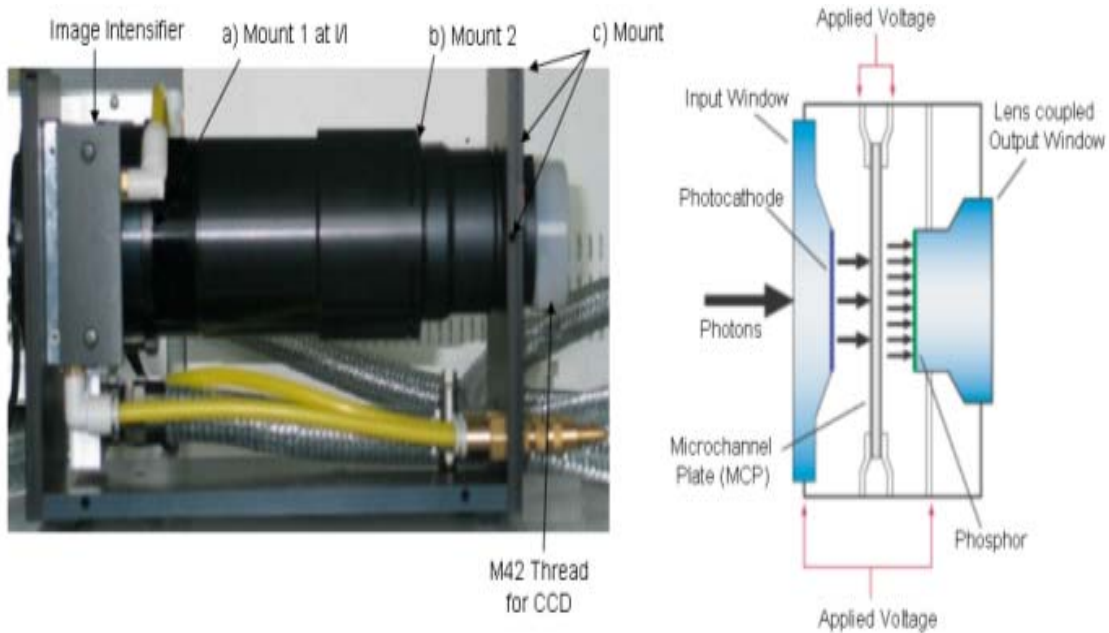


Figure 3.6 Internal structure of the intensifier.

The photo cathode basically converts the impinging photons into electrons. During the gate off period, the photo cathode field has a +50 V potential versus the MCP input surface. Due to potential difference the released photo electrons at the surface of photo cathode are pulled back to the photo cathode. Thereafter, in order to open the intensifier gate the polarity of the electric field is changed to -150 V, which in turn pushes the released photo electrons toward the MCP channels.

The MCP is a thin glass plate (0.5mm) with a large number of parallel channels (10 μ m diameter). Every electron entering a channel in the MCP collides with the channel wall and produces secondary electrons. Within the MCP channels these electrons are accelerated by high electric field gradient which results in further collision with the channel wall, producing further secondary electrons toward the phosphor screen.

The phosphor screen converts the electrons back into light photons again. The phosphor is covered by an aluminum surface which acts as a mirror in both directions. It reflects the back emitted light of the phosphor into the direction of the exit plane and also reflects residual light from the entrance surface that passed through the photocathode and the MCP.

3.1.5.2 CCD Camera

A charge-coupled device (CCD) is an analog shift register, which enables the transportation of analog signals (electric charges) through successive stages (capacitors) which is controlled by a clock signal. In a CCD, there is a photoactive region and a transmission region made out of a shift register [34].

An image is projected by a lens on the capacitor array (the photoactive region), causing each capacitor to accumulate an electric charge proportional to the light intensity at that location. A 2D array captures an object corresponding to the image projected onto the focal plane of the sensor. Once the array has been exposed to the image, a control circuit causes each capacitor to transfer its contents to its neighbor. The last capacitor in the array dumps its charge into a charge amplifier, which converts

the charge into a voltage. By repeating this process, the controlling circuit converts the entire semiconductor contents of the array to a sequence of voltages, which is transferred to the PCI-Board in the computer as a 12 bit data, which is saved in the computer where the operator decides further processing on them. With the Davis software the camera is controlled within the windows environment and the images are displayed on the monitor. Figure 3.7 depicts the CCD camera used for imaging during the laboratory phantom measurements.



Figure 3.7 CCD camera.

3.1.6 High Frequency Laser Synchronization

The sequence shown in figure 3.8 is the standard synchronization set-up for PicoStar camera system. In order to provide stable laser trigger an OCFD is used. Trigger signal is then fed into PC based HRI 150/350 delay card which passes a time shifted trigger signal to the HRI control unit. The camera is triggered by the HRI control unit and the subsequent laser pulse is captured by the intensifier gate depending on the laser trigger frequency.

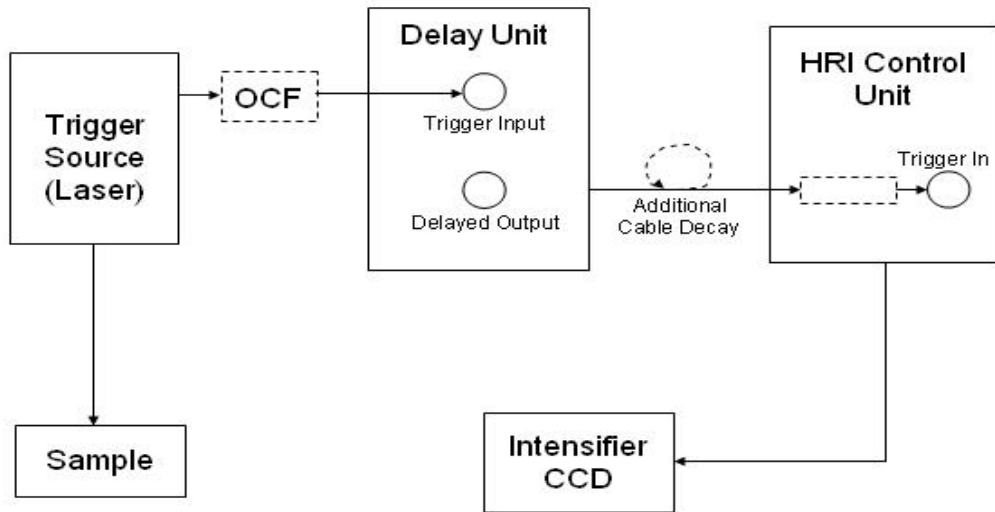


Figure 3.8 Block diagram of the imaging system.

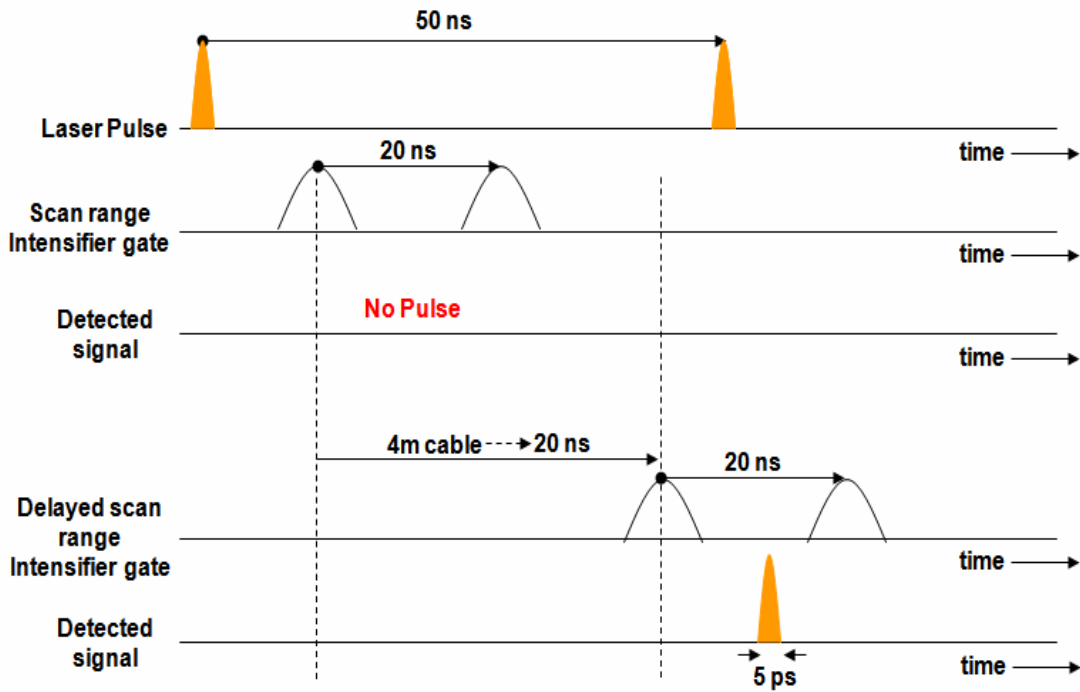


Figure 3.9 Timing diagram.

According to the system specifications, if the delay is not set larger than 2 ns, the delay unit has a limited scan range of 20 ns without jitter. For laser pulse

frequencies of 80 MHz this poses no problem. However, for lower frequencies of laser the time scan window range might mismatch the laser light profile. In figure 3.9 the scan range of the camera system is not aligned to the laser pulse giving an undesired small or no overlap to the laser profile. Using an additional cable delay between the delay card and HRI control unit, the time window of the scan range is shifted to give a good overlap with the laser profile (figure 3.9). In this study we have used the cable length of 5 meters to align the laser pulse within the scan range.

3.2 Phantom Setup

3.2.1 Preparation of the Model

In the modeling experiment, we used intralipid 20% which is a sterile, non-pyrogenic fat emulsion prepared for intravenous administration as a source of calories and essential fatty acids. It is made up of 20 % soybean oil, 1.2% egg yoke phospholipids, 2.25% glycerin and water for injection. In addition to this, sodium hydroxide is added to adjust the pH so that the final pH of the product is 8 [35]. Intralipid 20% was diluted to a concentration of 1% using distilled water to make a suspension which mimics the properties of the tissue reasonably well. The capillary with 150 mm long with 2.9 - 3.05 mm outer diameter and 1.5 – 1.6 mm bore (inner diameter) was placed in the intralipid medium which was taped with black tape to make its diameter 4 mm. The capillary was fixed onto a custom made plastic holder attached to a vernier height gage capable of measuring vertical movements with a precision of 0.02 mm.

Thereafter, the intralipid suspension was filled to the brim of the small plastic tub till it overflows into a bigger tub. Using the capillary holder and the height gage, the capillary was positioned at the surface of the suspension, such that the tube diameter-wise, was immersed in it. The position of the capillary filled with the ink capillary at this position was noticed. Then the capillary was moved to one mm from its initial position. In order to get the best possible focus, the ICCD camera was kept 20 cm away from the surface of the intralipid phantom. Camera was then focused at the surface of the intralipid using DC mode. The intralipid phantom was illuminated using the pulsed laser with minimal intensity and the intensity counts were monitored. Thereafter, intensity of the pulsed laser was increased gradually till the intensity count reached 3500 counts. Finally a CW image was captured in DC mode.

3.2.2 Data Acquisition in Time Gated Mode

ICCD camera specific Davis 7.0 software (LaVision Inc.) was used to control the image acquisition. First of all, the Davis 7.0 software was initialized. Thereafter, the parameters like MCP voltage, integration time, mode of acquisition (time-gated/DC), trigger threshold voltage, gate width and delay between the time gates were selected on the front panel of the Davis software.

Once these parameters were selected the camera shutter was kept closed and the dark image was grabbed. Thereafter, camera shutter was opened and all the measurements were taken in a dark room. Initially, to check the synchronization between the laser pulse and the delay, the delay was set at 0 ns position and the laser pulsed was searched in a step of 0.1 ns. Once found, the laser pulse was scanned

manually until it disappears and also intensity counts were checked in order to prevent any damage to the CCD sensor due to the high intensity. After assuring the appropriate intensity count, proper scan range and step size were selected and images were grabbed and saved using an automatic acquisition mode. Moreover, to get background images capillary was removed from the intralipid suspension and images were grabbed without changing the MCP voltage, integration time and scan range settings for a particular depth.

The level of capillary tube was then brought down by a millimeter into the suspension, using the vernier scale. The tub was again filled to the brim with the suspension to make sure that the surface level of the intralipid from which depth of the capillary was measured remained the same every time. Now the capillary was 1 mm below the previous depth (at 1 mm). Time gated images were again acquired for this depth. This process was repeated for every millimeter up to 9 mm and the image data acquired was stored in *.bmp format in the personal computer system. Figure 3.10 shows data sets generated for background and capillary at 1 and 2 mm depths. Moreover, in order to reduce experimental time CW image set for each depth was generated by adding respective time gated images.

After the data collection was done the time gated images with the capillary were divided by the corresponding time gated images without capillary using a Matlab script. Thereafter, these images were fitted for lorentzian curve using the least square fitting algorithm as discussed in section 2.4.2. Finally, comparisons of FWHM, contrast between the CW and time gated images were performed for all the depths.

Furthermore, the results for phantom study were compared with the Monte Carlo Simulations results. Figure 3.11 a, b, c, d and e shows a CW background image, a CW image with capillary at 2 mm depth, a CW ratio image, intensity profile of the ratio image and fitted lorentzian curve respectively.

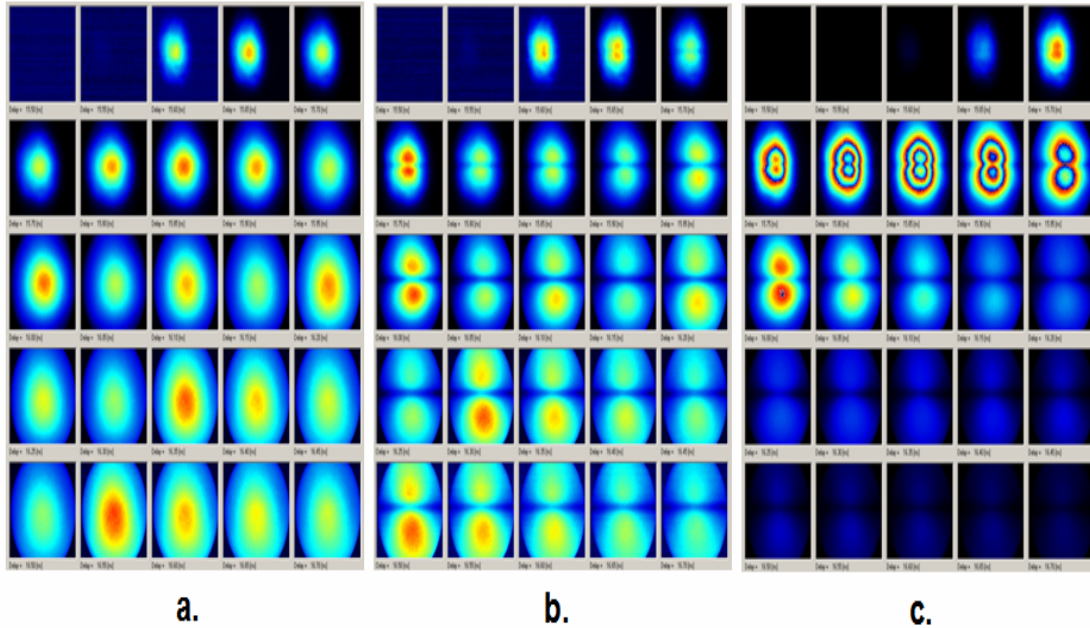
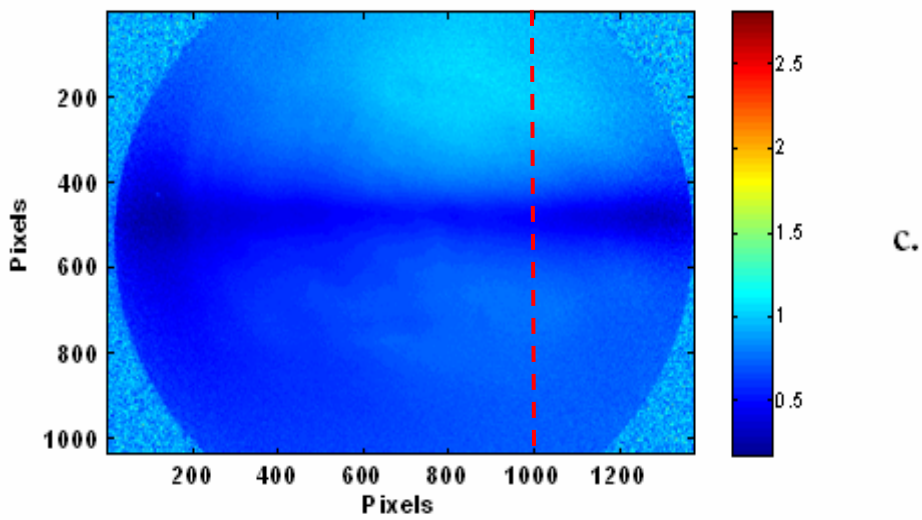
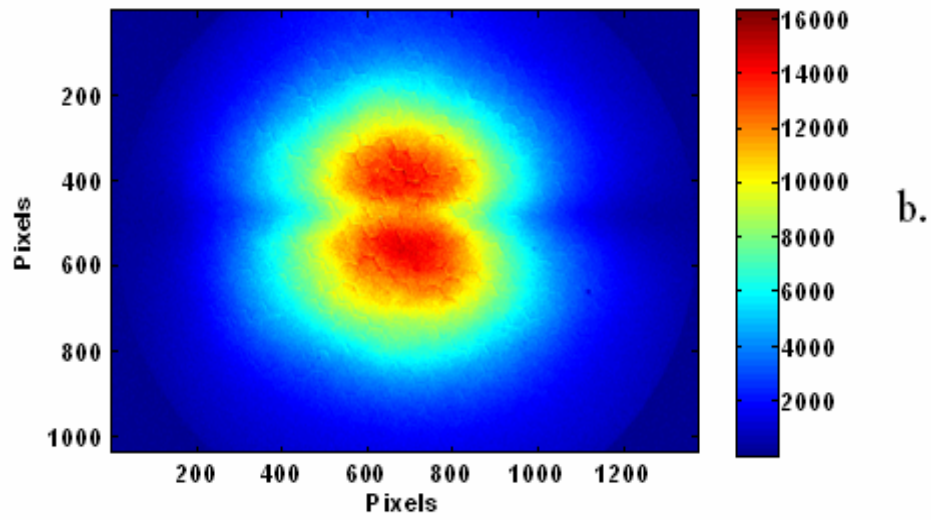
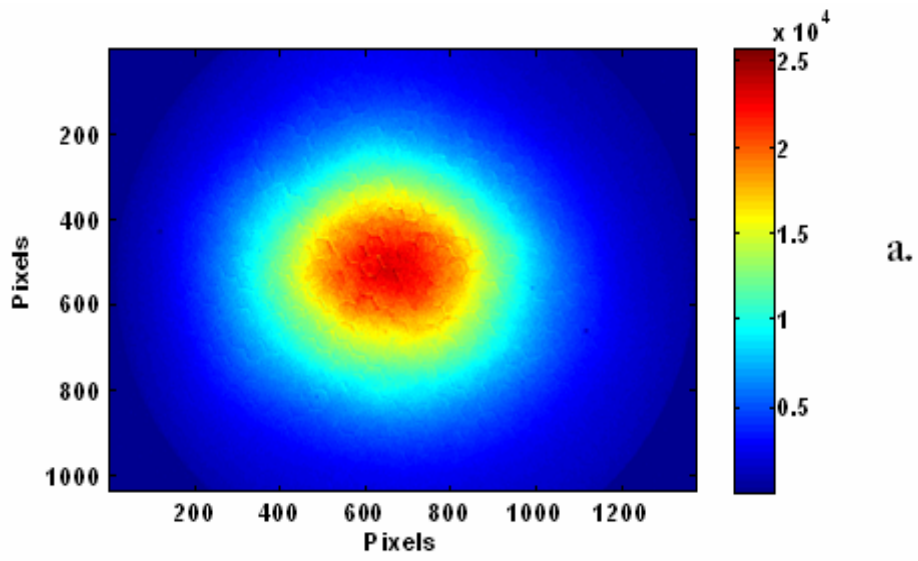


Figure 3.10 a) Time gated images for background. b) Time gated images for capillary at 1 mm. c) Time gated images for capillary at 2 mm.



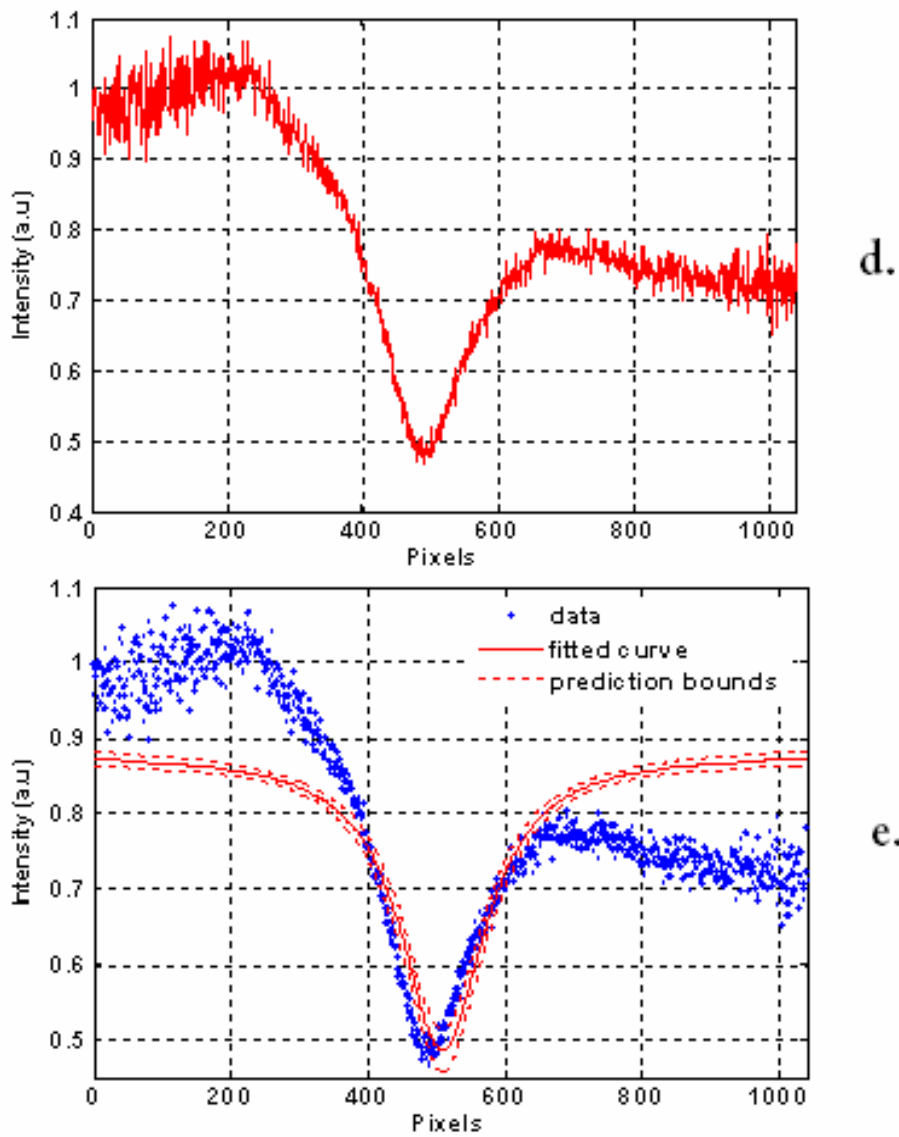


Figure 3.11 a) CW background image. b) CW image with capillary at 2 mm depth. c) CW ratio image. d) Intensity profile of the ratio image. e) Fitted lorentzian curve.

CHAPTER 4

RESULTS AND DISCUSSION

4.1 Monte Carlo Simulation Results

In order to analyze the sensitivity and resolution of the ICCD camera a feasibility study was performed using the Monte Carlo Simulations. Data was analyzed for different depth of the bile duct within the volume surrounded by the adipose tissue. As discussed earlier, the intensity profiles from the time gated images were gathered and fitted using the lorentzian function for each depth. Following sections discuss the comparison of contrast to background ratio and FWHM for time gated as well as Continuous Wave (CW) mode.

4.1.1 Contrast to Background Ratio (CBR)

Figure 4.1 shows the contrast to background ratio at each depth as a function of time for reflectance mode and 0.3 ns gate width. It can be noticed from the plot that the maximum ratio shift to the later times is a function of bile duct depth. The bile duct acts as an absorber for the light photons. Simulating the bile duct at different depth, in fact, delays the absorption event to the later time gates. Same result was found for 0.3 ns gate width. Figure 4.2 depicts the contrast to background ratio at each depth as a function of time for 0.3 ns gate width in transmission mode. Same results were found for the gate width of 0.03 ns for transmission and reflectance mode.

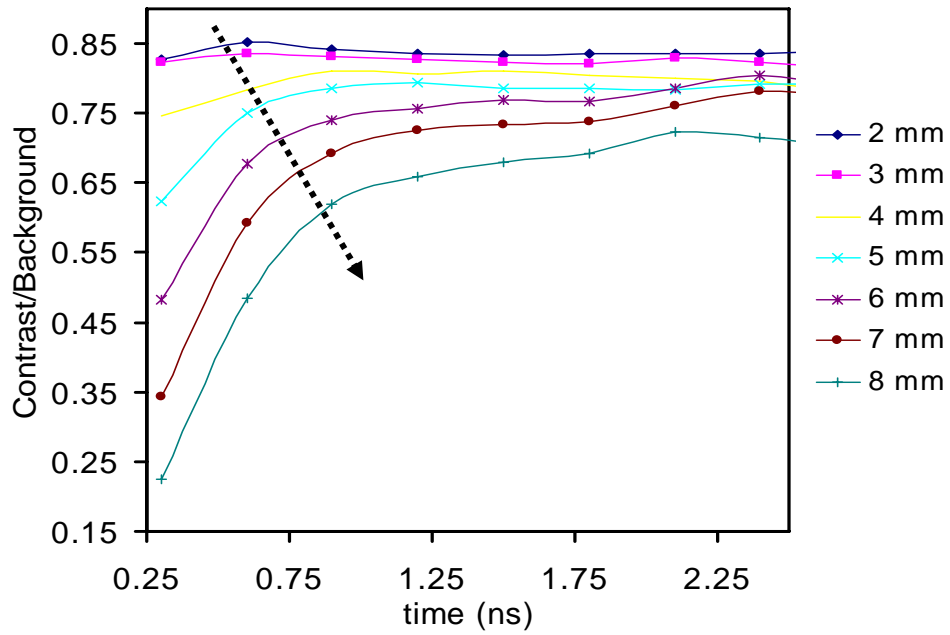


Figure 4.1 CBR for 0.3 ns gate width in reflectance mode.

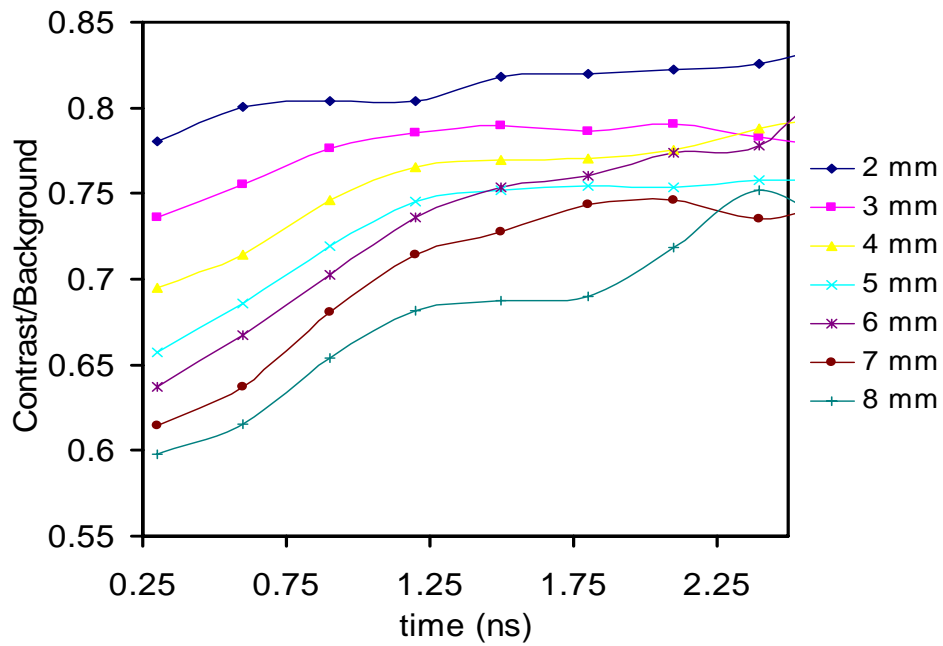


Figure 4.2 CBR for 0.3 ns gate width in transmission mode.

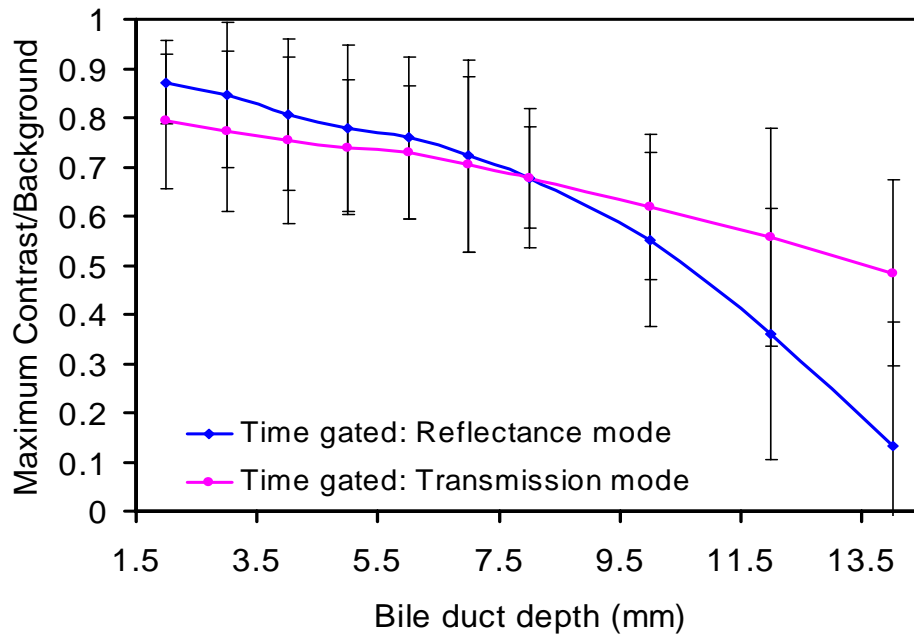


Figure 4.3 Comparison for maximum CBR between time gated reflectance and time gated transmission mode as a function of the bile duct depth, with 0.03 ns window gate.

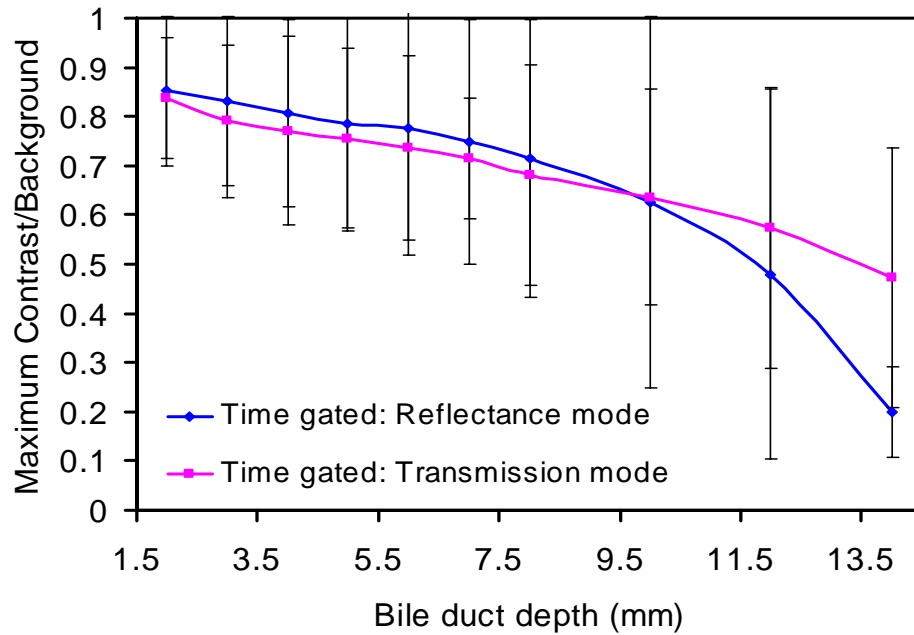


Figure 4.4 Comparison for maximum CBR between time gated reflectance and time gated transmission mode as a function of the bile duct depth, with 0.3 ns window gate.

Figure 4.3 and figure 4.4 show a comparison between maximum contrast to background ratio as a function of depth for time gated reflectance and transmission mode for 0.03 and 0.3 ns gates. Plots show that there is no much difference in terms of contrast to background ratio at shallower depths of the bile. However, at greater depths time gated transmission mode has higher sensitivity. Figure 4.5 and figure 4.6 show a comparison between maximum contrast to background ratio as a function of depth for CW reflectance and CW transmission mode, with 0.03 and 0.3 ns window gates. Plots depicts that the sensitivity of the CW transmission mode is superior as compared to that of CW reflectance mode. Moreover, CW contrast to background ratio decays faster with the increase in the bile duct depth and hence, it is difficult to detect the bile duct at the depth of 5 mm or greater in CW reflectance mode.

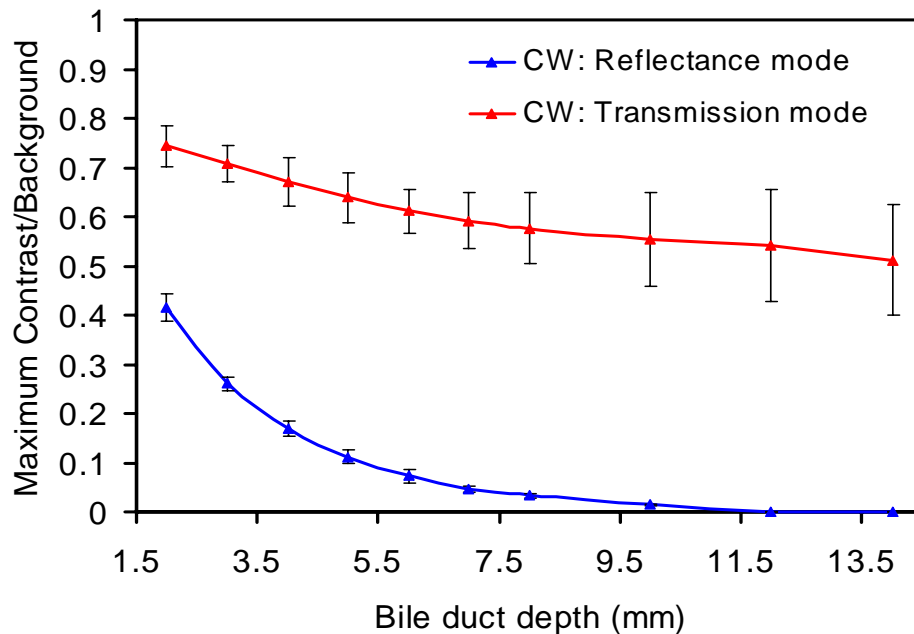


Figure 4.5 Comparison for maximum CBR between CW reflectance and CW transmission mode as a function of the bile duct depth, with 0.03 ns window gate.

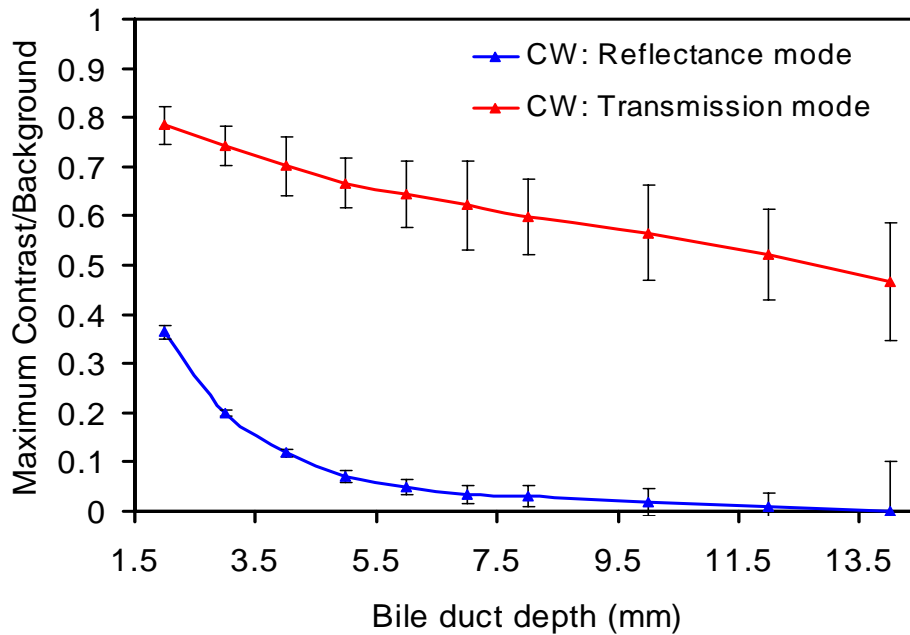


Figure 4.6 Comparison for maximum CBR between CW reflectance and CW transmission mode as a function of the bile duct depth, with 0.3 ns window gate.

Figure 4.7 and figure 4.8 show the relative comparison of contrast to background ratio for time gated reflectance and CW reflectance mode for the gate width of 0.03 and 0.3 ns respectively. It can be deduced from the plots that the time gated mode has greater sensitivity as compared to CW mode. Further, figure 4.9 and figure 4.10 show the comparison of contrast to background ratio for the time gated transmission and CW transmission mode for the gate width of 0.03 and 0.3 ns respectively. They also depict that in time gated and CW mode sensitivity is comparable at initial depths of the bile duct. For 4-8 mm of bile duct depth, time gated mode has higher sensitivity. However, the difference in sensitivity between the two imaging modes reduces at the greater depths of the bile duct because of scattering.

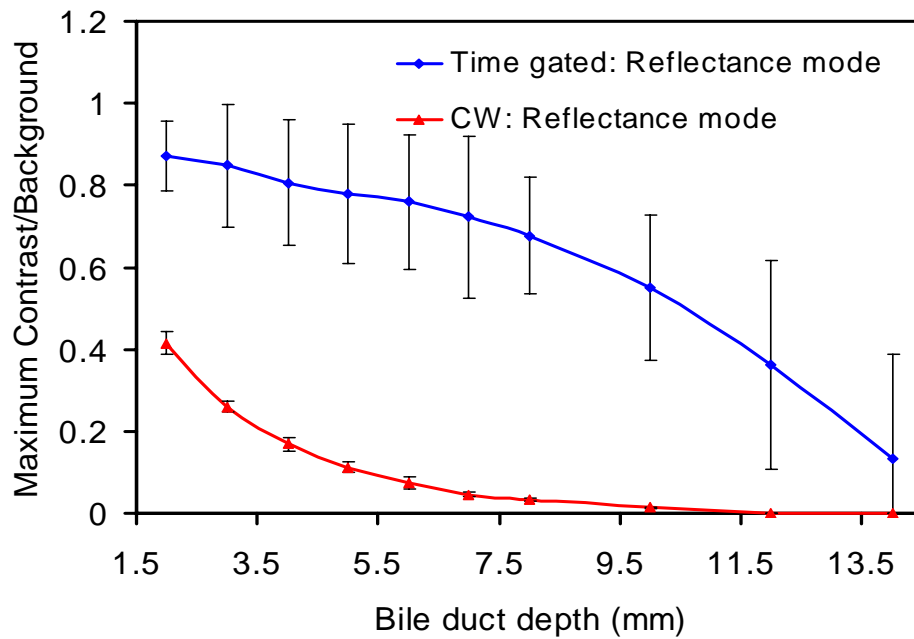


Figure 4.7 Comparison for maximum CBR between time gated reflectance (0.03 ns gate) and time gated transmission mode as a function of the bile duct depth.

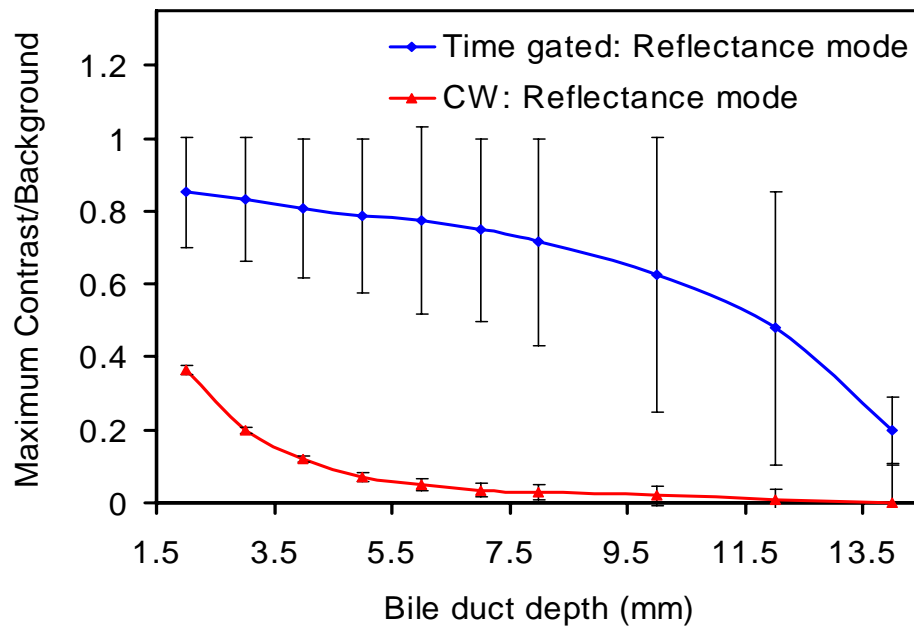


Figure 4.8 Comparison for maximum CBR between time gated reflectance (0.3 ns gate) and time gated transmission mode as a function of the bile duct depth.

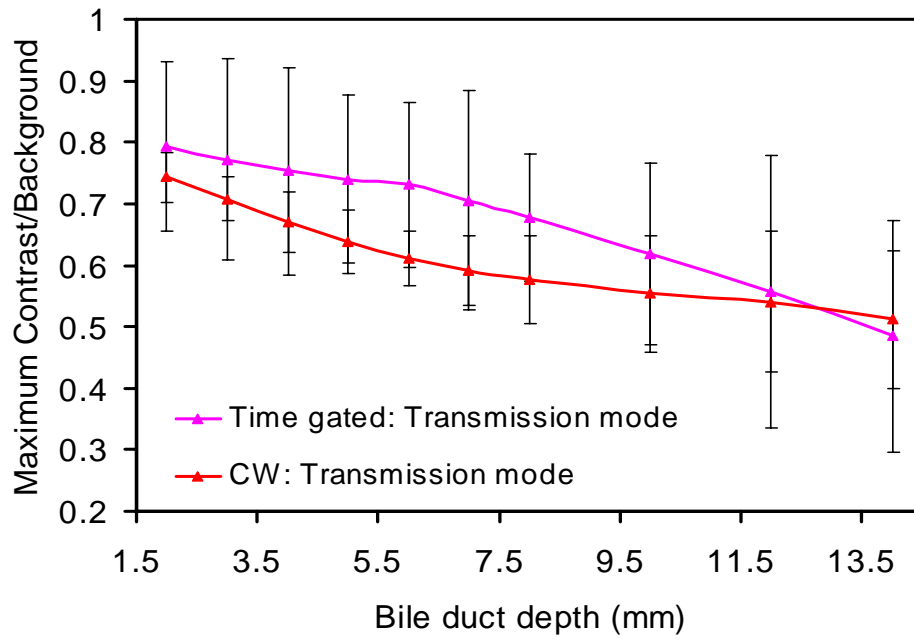


Figure 4.9 Comparison for maximum CBR between time gated reflectance (0.03 ns gate) and time gated transmission mode as a function of the bile duct depth.

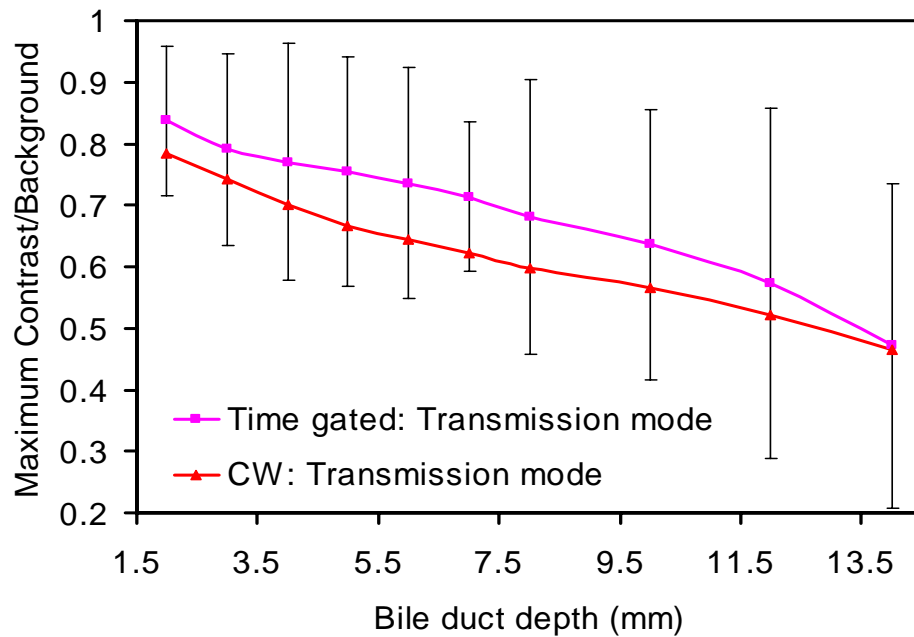


Figure 4.10 Comparison for maximum CBR between time gated reflectance (0.3 ns gate) and time gated transmission mode as a function of the bile duct depth.

4.1.2 Full Width at Half Maximum (FWHM)

FWHM is the parameter which determines the spatial resolution of the imaging system. As discussed in Chapter 2, a 4 mm diameter bile duct was imaged in the simulations and the change in the diameter (FWHM of the fitted lorentzian function) with the change in the bile duct depth was analyzed. Adipose is a scattering tissue type and as the photons penetrates the tissue; they undergo multiple scattering events which eventually results in broadening of the imaged object. Figure 4.11 and figure 4.12 show a comparison between minimum FWHM as a function of depth for time gated reflectance and time gated transmission mode for 0.03 and 0.3 ns gates respectively. It can be also noticed from the plots that the resolution for both the mode were same at initial depths of the bile duct. However, as the depth of the bile duct increases because of the light photon scattering in reflectance mode the shadow of the bile duct appears broader as compared to transmission mode. Hence, time gated transmission mode has an edge over time gated reflectance mode in terms of resolution at greater bile duct depths.

Figure 4.13 and figure 4.14 show a comparison between minimum contrast as a function of the bile duct depth for 0.03 ns and 0.3 ns gate width respectively. Both the plot follows the same trend. Furthermore, the plots suggest that the difference in spatial resolution for CW transmission and reflectance mode is not as big as in time gated mode reflectance and transmission mode.

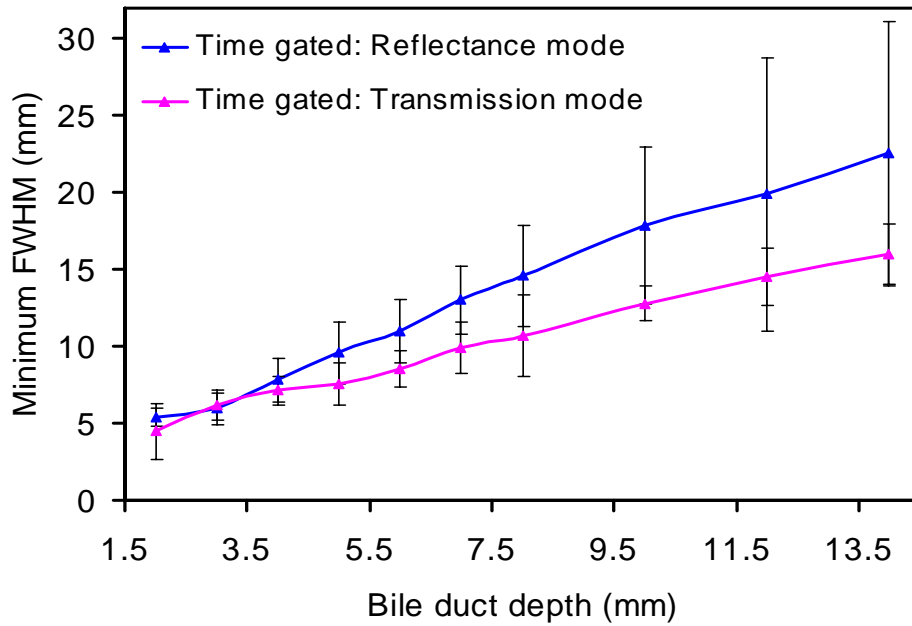


Figure 4.11 Comparison for minimum FWHM between time gated reflectance and time gated transmission mode as a function of the bile duct depth.

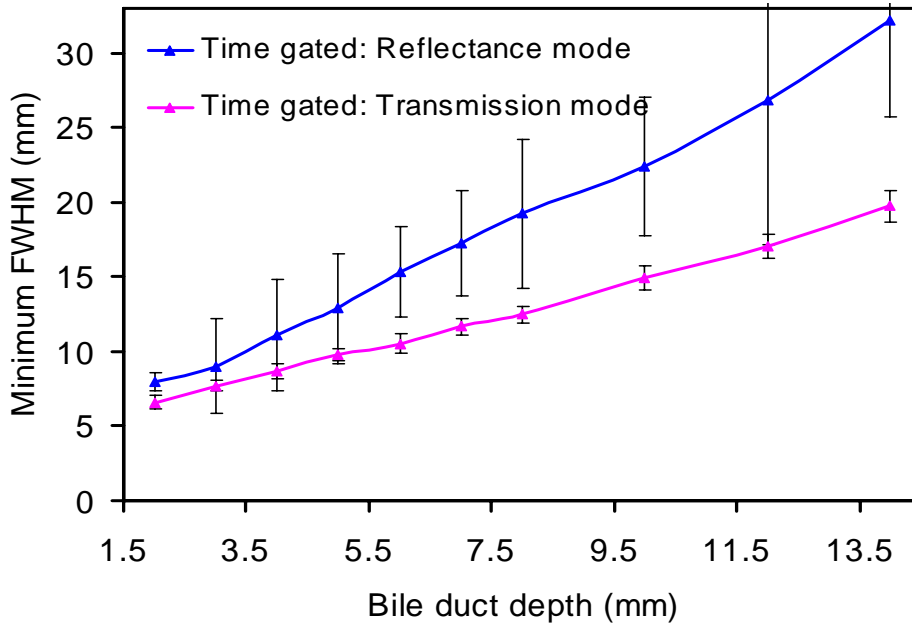


Figure 4.12 Comparison for minimum FWHM between time gated reflectance and time gated transmission mode as a function of the bile duct depth.

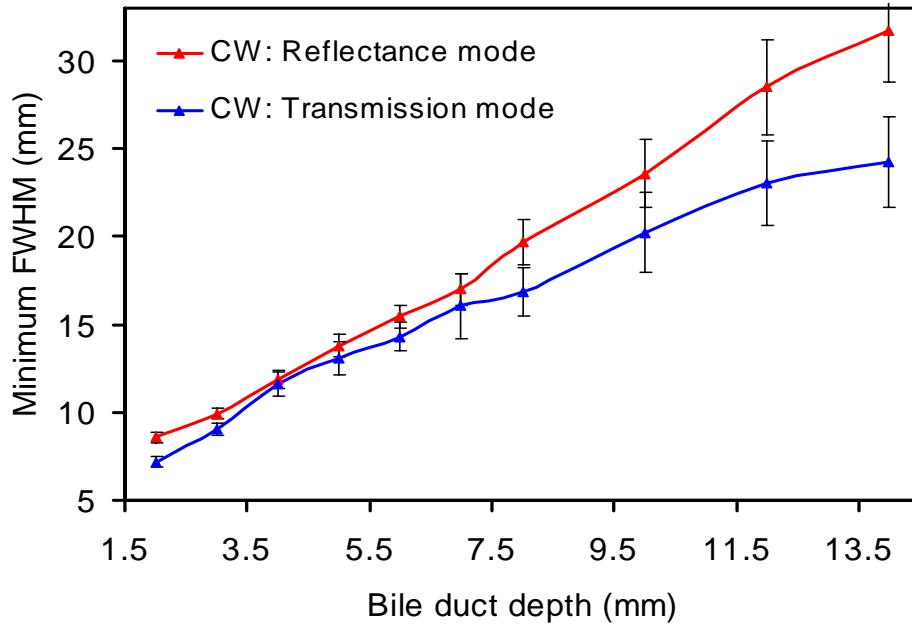


Figure 4.13 Comparison for minimum FWHM between CW reflectance and CW transmission mode as a function of the bile duct depth.

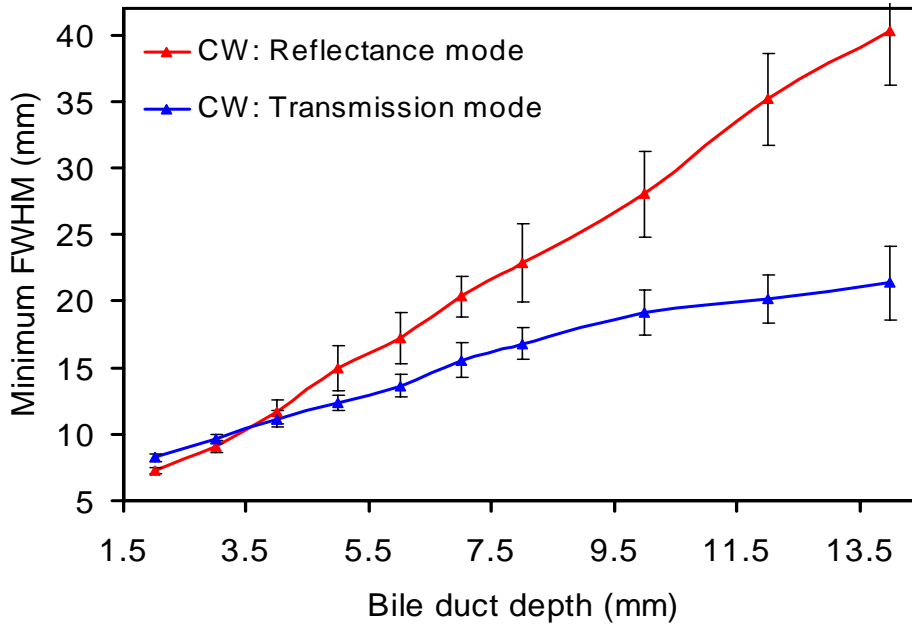


Figure 4.14 Comparison for minimum FWHM between time gated reflectance and time gated transmission mode as a function of the bile duct depth.

Figure 4.15 and figure 4.16 is a relative comparison for spatial resolution change as a function of the bile duct depth for time gated reflectance and CW reflectance mode for 0.03 and 0.3 ns gate width respectively. The same comparison for the transmission mode is shown in figure 4.17 and figure 4.18 respectively. In both the cases FWHM for time gated and CW mode was closer for initial depths of the bile duct. However after 3 mm the time gated mode starts gaining superior resolution as compared to CW mode. Moreover, spatial resolution was superior in time gated mode as compared to CW mode and hence the object imaged using time gated imaging appear closer to its actual physical size. Hence, it can be concluded that the time gated mode in transmission as well as in reflectance mode has an edge over CW transmission and CW reflectance mode in terms of spatial resolution.

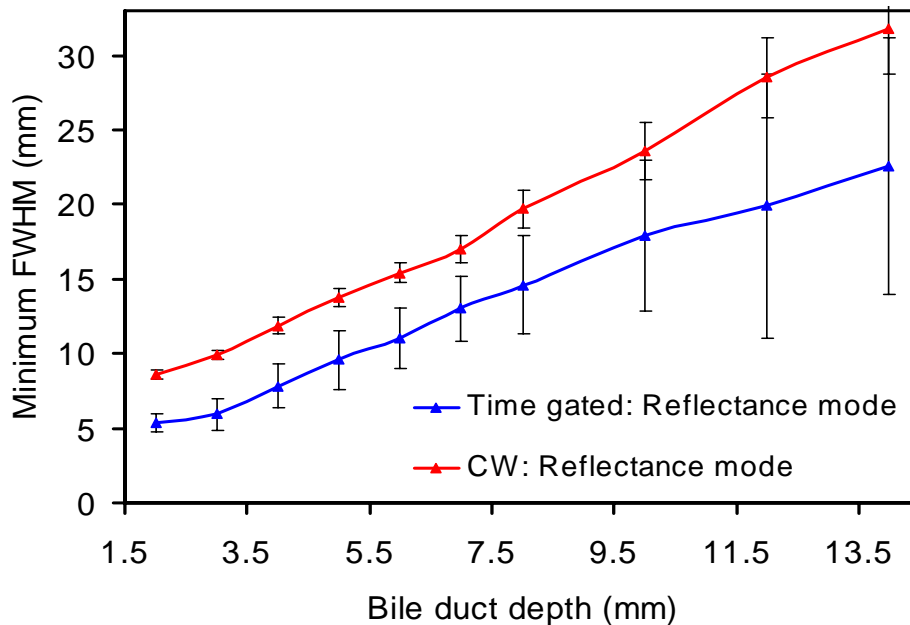


Figure 4.15 Comparison for minimum FWHM between time gated reflectance mode (0.03 ns gate) and CW reflectance mode as a function of the bile duct depth.

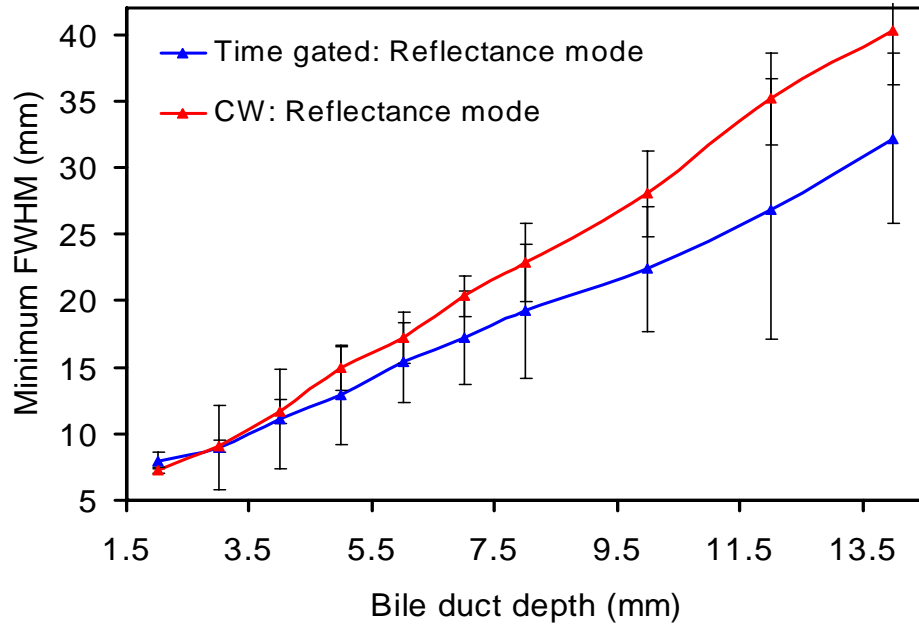


Figure 4.16 Comparison for minimum FWHM between time gated reflectance mode (0.3 ns gate) and CW reflectance mode as a function of the bile duct depth.

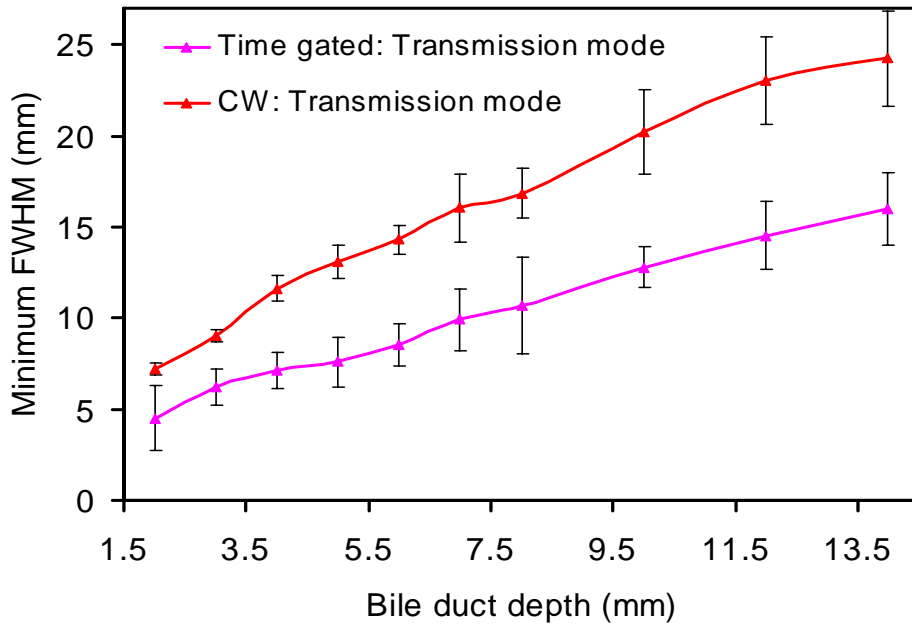


Figure 4.17 Comparison for minimum FWHM between time gated transmission mode (0.03 ns gate) and CW transmission mode as a function of the bile duct depth.

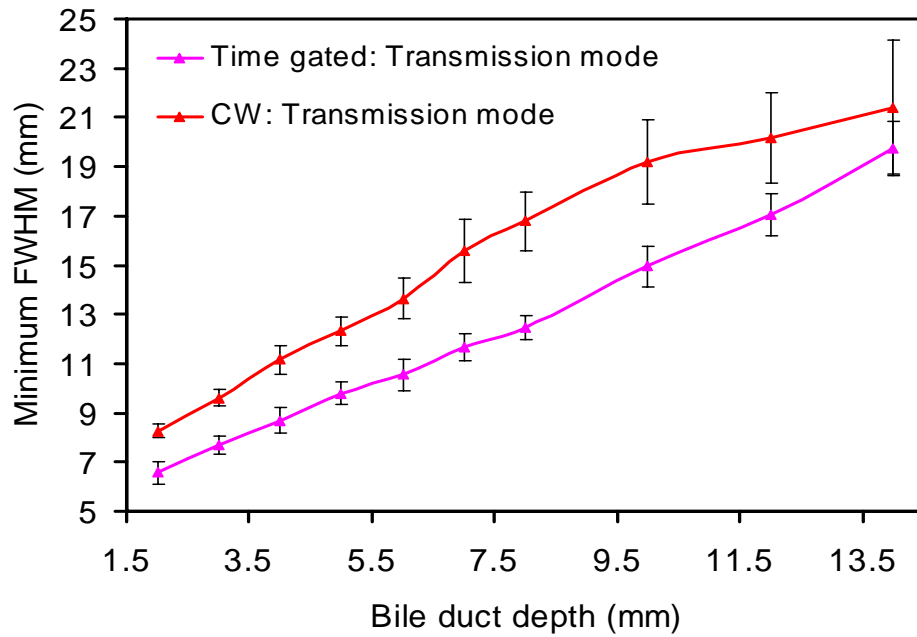


Figure 4.18 Comparison for minimum FWHM between time gated transmission mode (0.3 ns gate) and CW transmission mode as a function of the bile duct depth.

4.2 Phantom Study Results

4.2.1 Contrast to Background Ratio and Full Width at Half Maximum

Apart from the Monte Carlo Simulations, in order to test the feasibility of the time gated imaging system, laboratory phantom studies were performed. As discussed in chapter 3 all the measurements were performed with a fixed gate width of 0.3 ns. Moreover, 0.05 ns, 0.1 ns and 0.3 ns step size were used to generate three different data sets for each depth of the absorber (Figure 4.19).

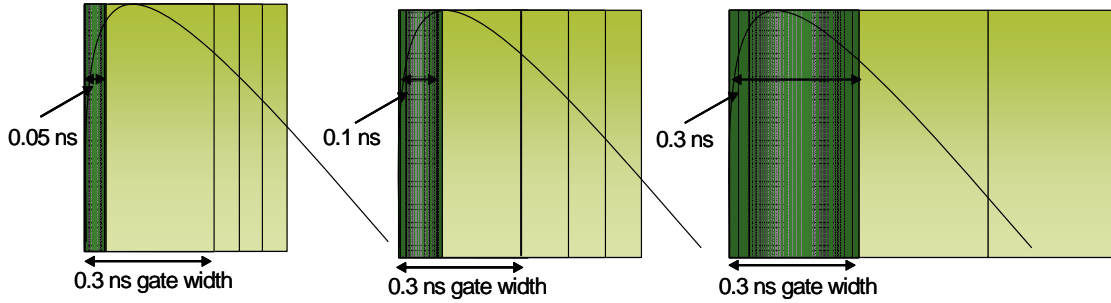


Figure 4.19 Schematic showing different step size (0.05 ns, 0.1 ns and 0.3 ns) with a fixed gate width of 0.3 ns.

Figure 4.20, figure 4.21 and figure 4.22 show the contrast to background ratio at each depth of the absorber as a function of time for reflectance mode, 0.3 ns gate width and the step size of 0.05 ns, 0.1 ns and 0.3 ns respectively. As discussed in the previous section the maximum contrast to background ratio shifts to the later times with the absorber depth. Same trend was seen with 0.05 ns, 0.1 ns and 0.3 ns step size. As the banana penetrates the center of the absorber maximum contrast to background ratio occurs at that time gate and at the later time gates the photon banana contains less information from the absorber and the detected signal is dominated by the surrounding medium. Hence, the contrast to background ratio decays after reaching the peak. Furthermore, in order to check the effect of step size on the contrast to background ratio two absorber depths (1 mm and 3 mm) were picked for all three step sizes (0.05 ns, 0.1 ns and 0.3 ns) and plotted as figure 4.23 and figure 4.24 respectively. It can be noticed from the plot that the larger step size reduces the number of data points required to scan the imaged object and hence reduces the noise at the cost of resolution. However, step size does not make difference to the sensitivity of the imaging system.

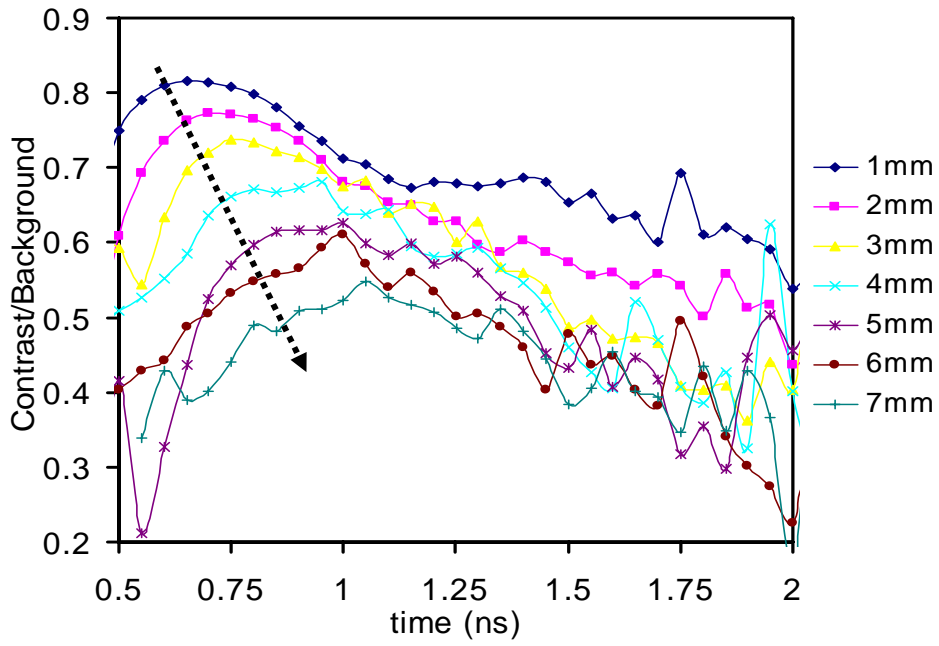


Figure 4.20 CBR for 0.3 ns gate width and step size of 0.05 ns.

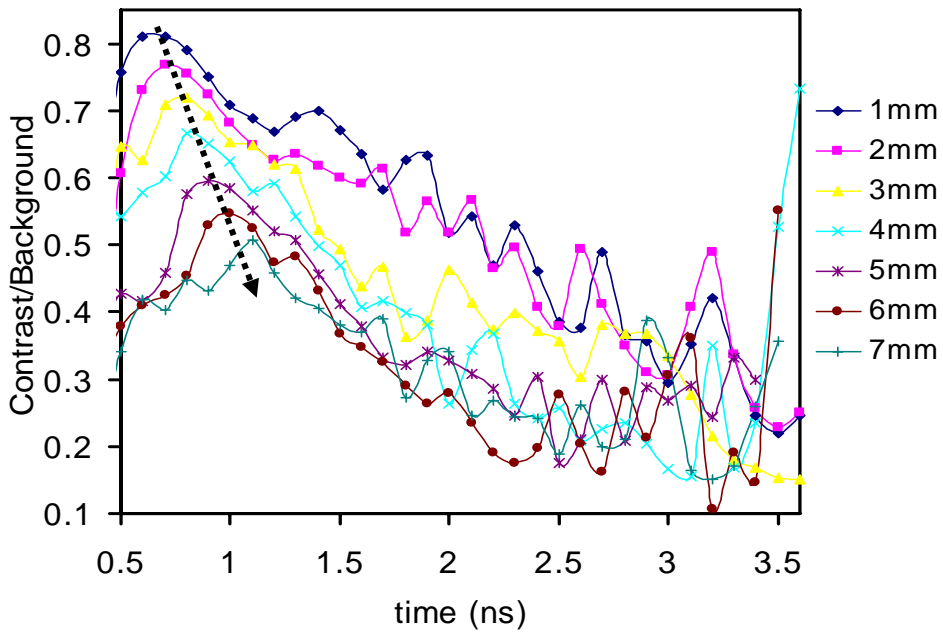


Figure 4.21 CBR for 0.3 ns gate width and step size of 0.1 ns.

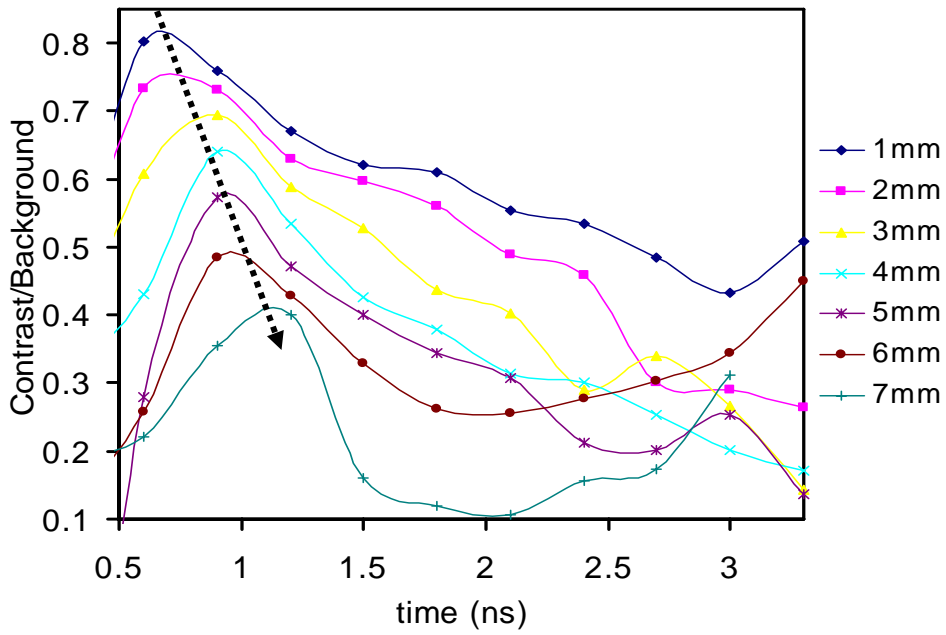


Figure 4.22 CBR for 0.3 ns gate width and step size of 0.3 ns.

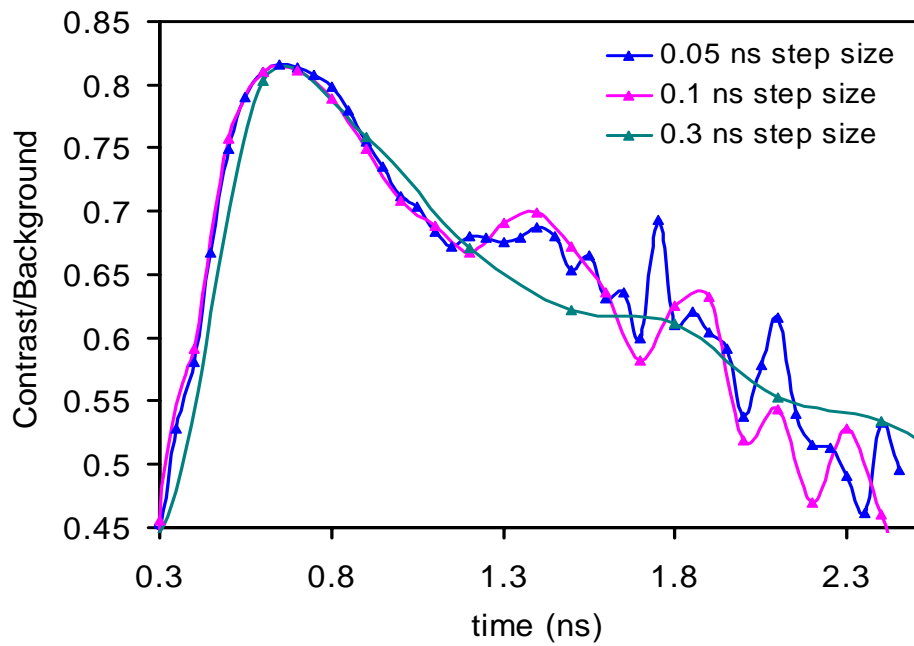


Figure 4.23 Comparison of CBR in reflectance mode for absorber at 1 mm, gate width of 0.3 ns and step size of 0.05 ns, 0.1 ns, 0.3 ns.

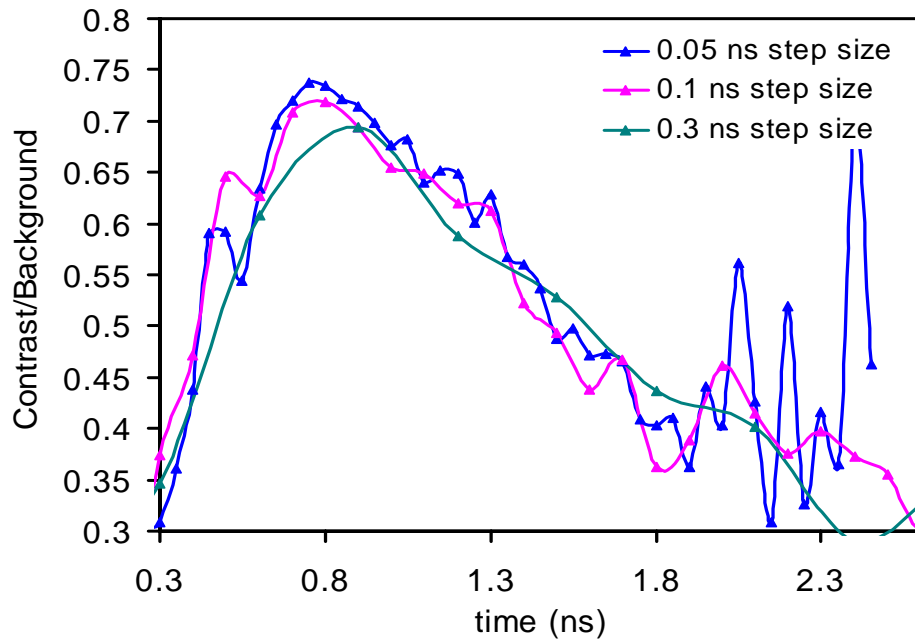


Figure 4.24 Comparison of CBR in reflectance mode for absorber at 3 mm, gate width of 0.3 ns and step size of 0.05 ns, 0.1 ns, 0.3 ns.

For further processing these data sets were used. In order to analyze the sensitivity of the imaging system as a function of absorber depth the maximum points from the curves (figure 4.20, 4.21 and 4.22) were picked at each depth of the absorber and plotted as a function of absorber depth (figure 4.25). Moreover, student t-test was performed between the maximum contrast to background values for 0.05 ns and 0.1 ns step size and also between the 0.1 ns and 0.3 ns step size. The p-values found for both the cases were 0.58 and 0.76 respectively, which are significantly higher than the critical value ($\alpha=0.05$), which support the fact that the step size does not affect the sensitivity of the imaging system. Comparison for the change in contrast to background ratio between time gated and CW mode was not done as the curve fitting was not good for CW mode. Moreover, same analysis was done to determine spatial resolution of the

imaging system. Plot in the figure 4.26 shows the FWHM for time gated reflectance mode at different step size. The plot depicts that at shallower depths, the size of the imaged absorber appears closer to it actual size. However, at greater depths because of light scattering the shape gets broaden results in poor spatial resolution. Moreover, FWHM for three different step sizes shows the same trend. Student t-test was performed between the FWHM values for 0.05 ns and 0.1 ns step size and also between the 0.1 ns and 0.3 ns step size. The p-values found for both the cases were 0.99 and 0.94 respectively, which are significantly higher then the critical value ($\alpha=0.05$), which support the fact that the step size does not effect the resolution of the imaging system.

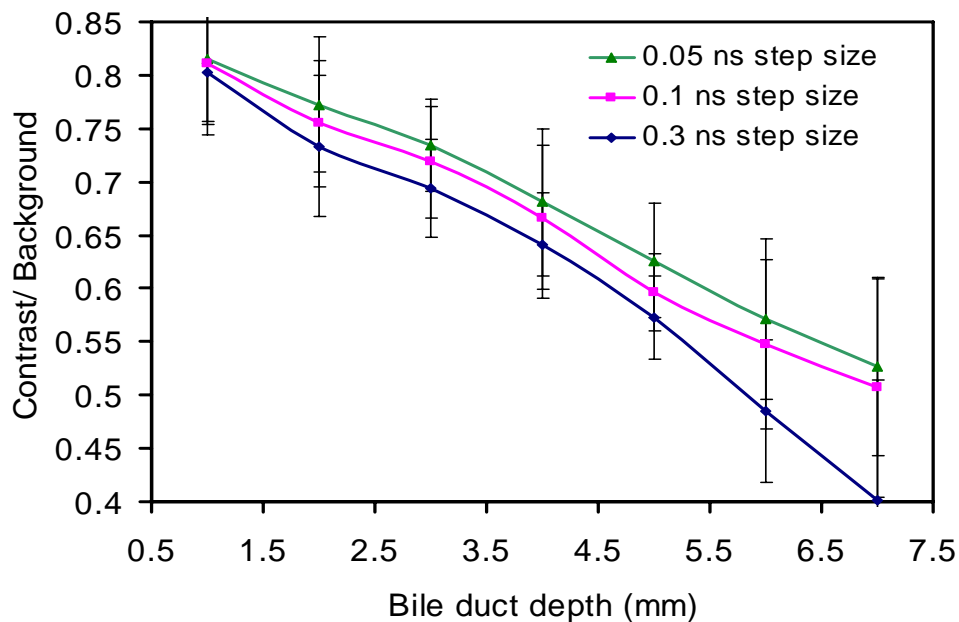


Figure 4.25 Comparison for maximum CBR for time gated reflectance (gate width 0.3 ns) at different step sizes (0.05 ns, 0.1 ns and 0.3 ns).

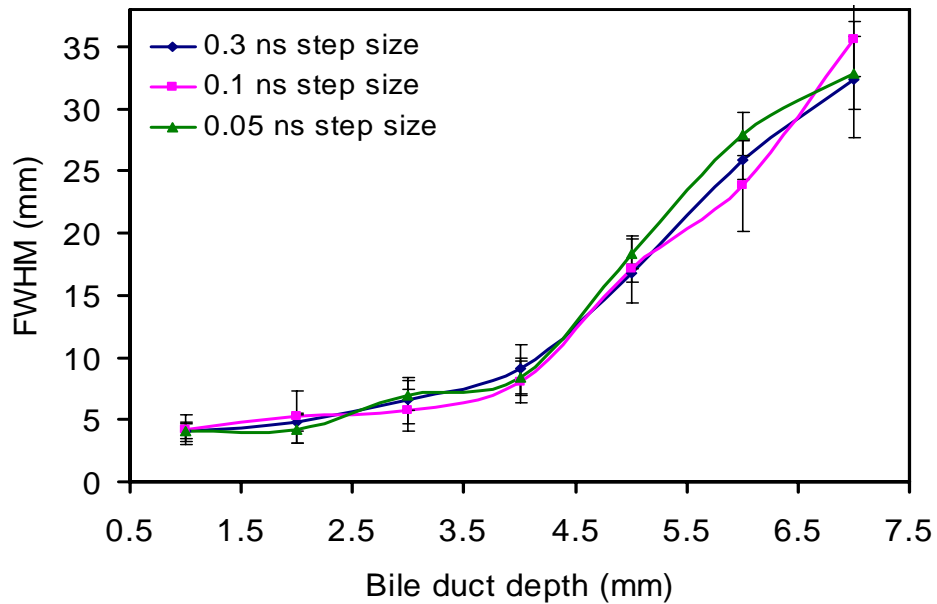


Figure 4.26 Comparison for FWHM for time gated reflectance (gate width 0.3 ns) at different step sizes (0.05 ns, 0.1 ns and 0.3 ns).

4.3 Comparison between Experiments and Monte Carlo Simulations

In order to validate the Monte Carlo Simulations results with experimental data we chose the experimental data with 0.3 ns gate width, 0.05 ns step size and absorber at 2 mm depth. Moreover, for Monte Carlo Simulations, data with the 0.3 ns gate width and the bile duct at 2 mm was chosen for the comparison. Figure 4.27 shows the change in contrast to background ratio as a function of time for experimental and Monte Carlo Simulations. The plot suggests that the contrast to background ratio reaches the peak at the same time. However, for experimental data, the ratio (contrast/ background) decays faster whereas the ratio (contrast/ background) for Monte Carlo Simulations decays much slower once the peak was reached.

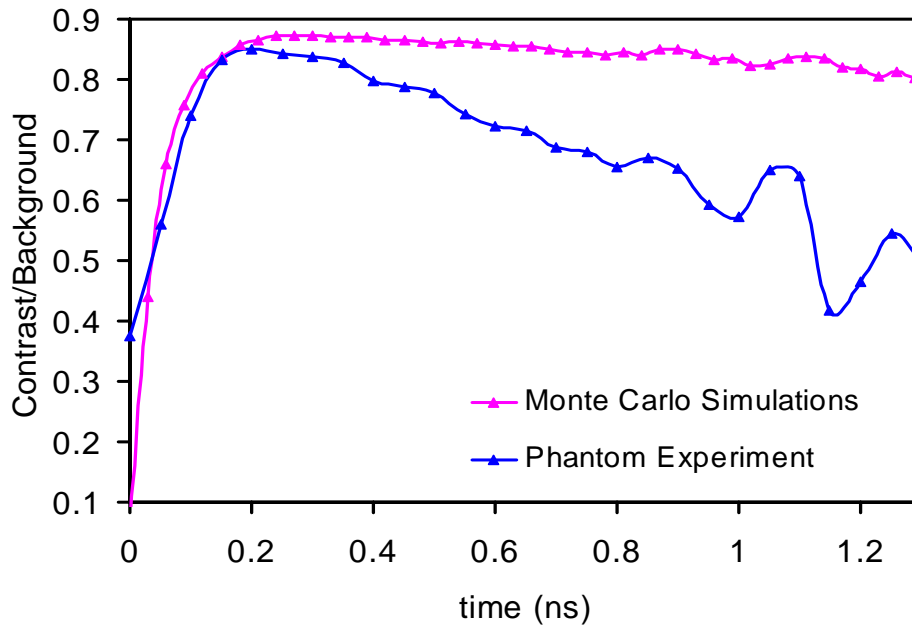


Figure 4.27 Comparison for CBR between Monte Carlo Simulations (bile duct at 2 mm) and the phantom experiment (absorber at 2 mm).

One reason could be the mismatch between the experimental setup and the simulated geometry. For Monte Carlo Simulations the dimensions for the simulations was 100 X 100 X 20 mm and in phantom experiments the container dimensions was 150 X 100 X 100 mm. Moreover, the difference in optical properties of the simulated bile duct in Monte Carlo Simulations and the absorber used in the phantom experiments could be the possible reason for the mismatch. In order to match the simulations with the phantom experiments, geometry of the Monte Carlo Simulations was changed as shown in figure 4.28. Simulations were performed for the bile depth of 2 mm and 4 mm. Same data processing steps were employed as before and the contrast to background ratio as a function of time was plotted and compared with the same of the

previous geometry for the bile ducts depths of 2 mm and 4 mm. Figure 4.29 and figure 4.30 show the comparison. It can be noted from the plots that the contrast to background ratio decays faster with the modified geometry but the change is not significantly large enough as compared to the experimental data. Thus, the effect of simulation geometry could not be the main reason for the mismatch between the experiments and the simulations. Finally, to match the optical properties of the black absorber used for the experiments, simulations were performed again with the old geometry and modified μ_a value (10 times higher than its previous value) and 0.3 ns gate width with the bile duct at 2 mm and 4 mm. The data was analyzed. There was no change in simulated data

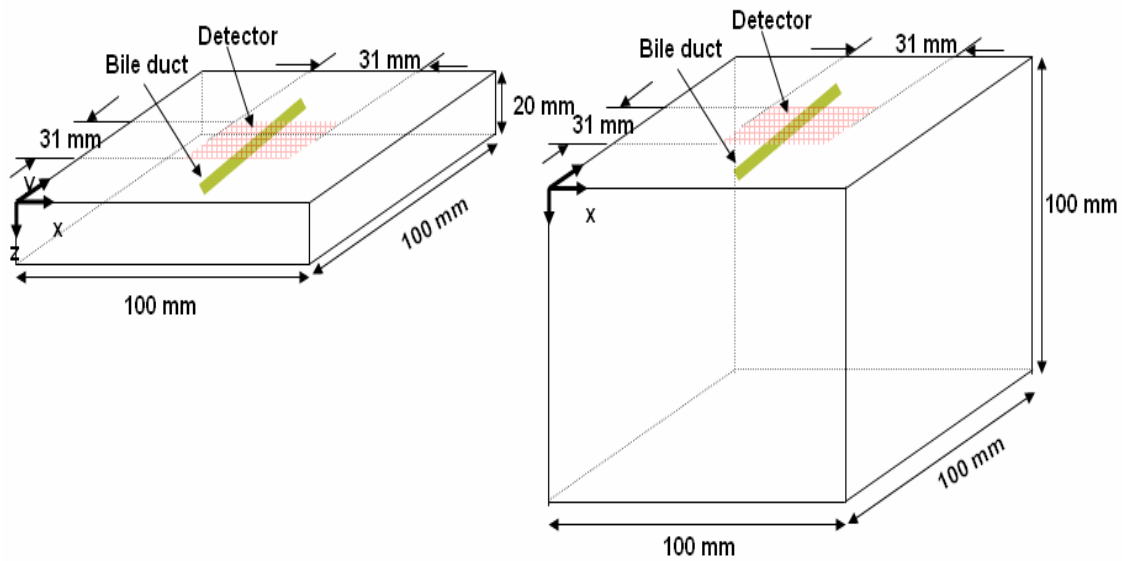


Figure 4.28 Schematic showing original simulation geometry (left) and modified simulation geometry (right) used to match the experimental data with the simulation data.

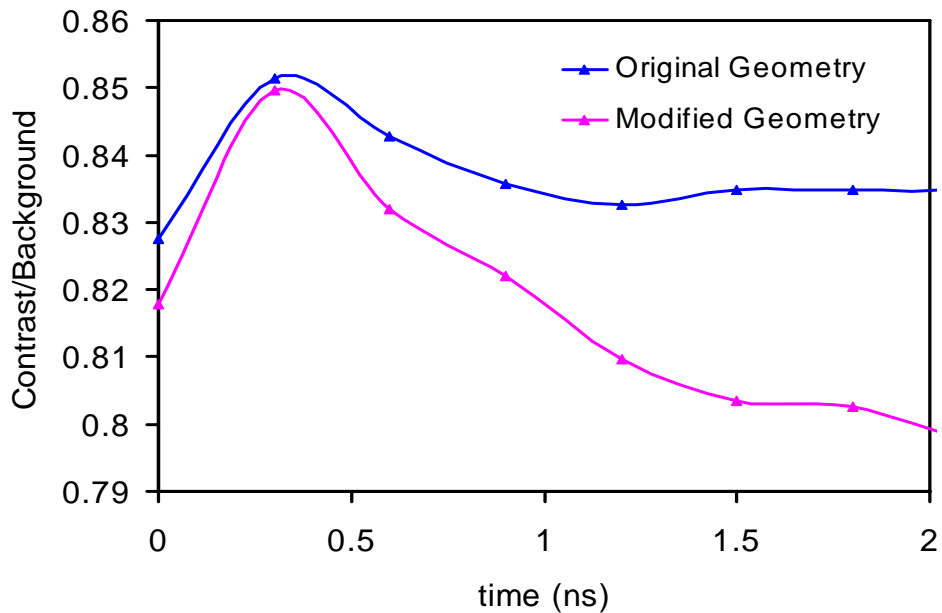


Figure 4.29 Comparison for CBR for original and modified simulation geometry with a bile duct at 2 mm depth.

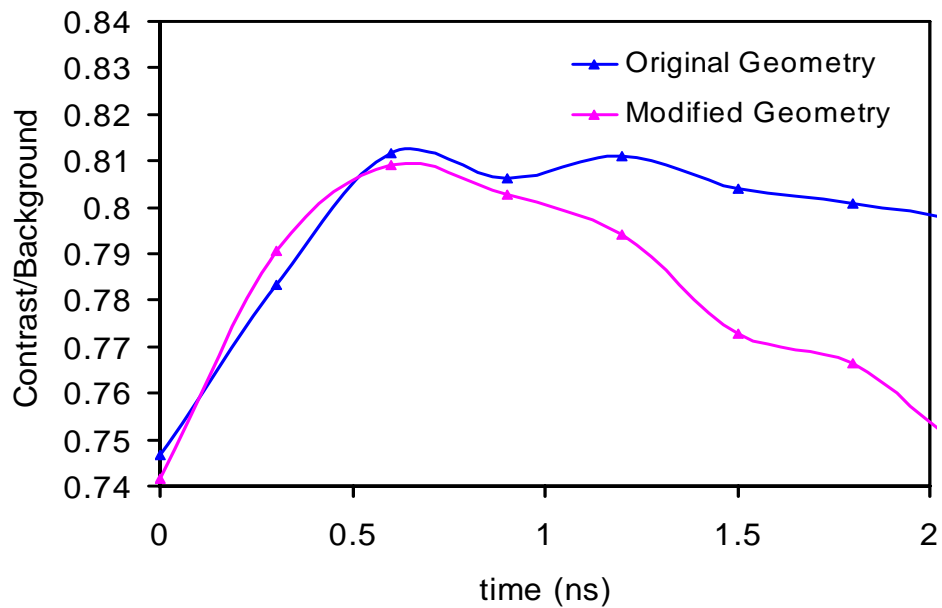


Figure 4.30 Comparison for CBR for original and modified simulation geometry with a bile duct at 4 mm depth.

CHAPTER 5

CONCLUSION

From the experiments and Monte Carlo Simulations, I conclude that the sensitivity of the CW transmission mode is higher by ~40% as compared to reflectance mode. Hence we can see that if CW imaging is used it would be better to use in transmission mode. Moreover, time gated reflectance mode has ~30% higher sensitivity as compared to CW reflectance mode while the sensitivity of the time gated imaging is comparable to CW imaging in the transmission mode. Hence, it is better to use time gated reflectance mode to gain higher sensitivity if reflectance mode is utilized. Spatial resolution of CW and time gated mode was comparable at shallower depths; however, at greater depths time gated mode has an edge over CW mode for transmission as well as reflectance mode. Overall, the time domain imaging system has an edge over CW imaging technique in terms of sensitivity and spatial resolution.

In my study, I observed that the maximum sensitivity (i.e. maximum contrast) and the best spatial resolution do not occur at the same time gate. Specifically, I observed that the maximum contrast occurs at the middle time gates during the temporal scan, at which the absorber is located near the center of a banana profile (i.e., the most probable photon traveling paths between the source and detector). However, the best spatial resolution (i.e., minimum FWHM) was observed at the earlier time gates where the banana profile just penetrates the tip of the absorber and results in a smaller

FWHM. Hence, there is a tradeoff between the sensitivity and spatial resolution of the time gated imaging system.

The match between the phantom experiments and Monte Carlo Simulations were not found to be exact. The reason for the mismatch at the later gated times is unclear to me at the present time. Further investigations on the experimental setups and Monte Carlo Simulation are needed to understand the mismatch.

For the overall study, one can improve the experiments by performing the measurement in transmission mode and using bile as an absorber rather than using ink within the phantom. Improvements for the Monte Carlo Simulation can include a more robust fitting algorithm and change in the illumination pattern and the perfect size selection of the phantom.

APPENDIX A
MATLAB SCRIPTS

MATLAB code for generating voxelized model

```
close all;
clear;
clc;

ModelFilename = 'bile_2mm.bin'; % Input file name
[fid, message] = fopen(ModelFilename,'w'); % Opening file to write

dx = 1 % Define voxel size (mm)

nxvox = 100; % no. of voxel in x direction
nyvox = 100; % no. of voxel in y direction
nzvox = 20; % no. of voxel in z direction

voxel(1:nxvox,1:nyvox,1:nzvox) = 0; %air
voxel(2:nxvox-1,2:nyvox-1,2:nzvox-1) = 1; %adipose
voxel(2:nxvox-1,51:54,3:6) = 2; %bile duct
voxel(2:nxvox-1,51:51,3:3) = 1;
voxel(2:nxvox-1,54:54,3:3) = 1;
voxel(2:nxvox-1,51:51,6:6) = 1;
voxel(2:nxvox-1,54:54,6:6) = 1;

for z = 1 : nzvox
    for x = 1 : nxvox
        for y = 1 : nyvox
            count = fwrite(fid,voxel(x,y,z),'char'); % writing file
        end
    end
end

fclose(fid);
```

MATLAB code for reading voxelized model

```
close all;
clear;
clc;

[fid, message] = fopen('bile_2mm.bin','r','a'); % Input file name
stream = fread(fid,'char'); % Opening file to read

nxvox = 100 ; % no. of voxel in x direction
nyvox = 100 ; % no. of voxel in y direction
nzvox = 20 ; % no. of voxel in z direction

for z = 1:nzvox
    for x = 1:nxvox
        for y = 1:nyvox
            I(z,y,x) = stream((z-1)*nxvox*nyvox + (x-1)*nyvox + y);
        end
    end
end

direction = ['y' 'x' 'z' 'z' 'z'];
position = [21 10 16 10 18]; % giving parameters to cut in x, y, z direction
for i = 1 : length(direction)
    switch direction(i)
        case 'x'
            II = permute(I, [1 2 3]);
            section = II(:, :, position(i));
        case 'y'
            II = permute(I, [1 3 2]);
            section = II(:, :, position(i));
        case 'z'
            II = permute(I, [2 3 1]);
            section = II(:, :, position(i));
    end

    figure('color','w');
    imagesc(section); colorbar; grid; % image
    cut = sprintf('Profile: %s = %d', direction(i), position(i));
    title(cut);
end

fclose(fid)
```


MATLAB code for reading "*.his file"

```
close all;
clear;
clc;

% no of photons inserted
Nphoton = 15*10^7;
Pi = 3.14;
rad = 0.5; % radius 0.5 mm
t = 0.03; % gate width

% tissue property: mua mus g n
tissue = [ 5.19e-3 1.133 0.01 1.4    % adipose
          0.3    0.625  0.01 1.4 ] % bile

% tissue property to generate background file
%tissue = [ 5.19e-3 1.133 0.01 1.4    % adipose
           5.19e-3 1.133 0.01 1.4 ] % adipose

Ngate = 50; %total no. of time gate
det_x = 31; % no. of detector in x direction
det_y = 31; % no. of detector in y direction
detector = det_x*det_y; %total no of detector
a = zeros(detector,Ngate); % initalizing 2D array
[Ntissue ysize] = size(tissue);
mua = tissue(:,1);
SegLength = 2+Ntissue;

% Reading file
[fid, message] = fopen('2mm_bile.his','r','a');
b = fseek(fid,-1,'eof'); % Getting EOF
c = ftell(fid);
frewind(fid); % Placing FP to initial position
i = 0; x = 0; y = 0; z = 0;
% reading file till end
while ~ feof(fid)
    i = i+1;
    % if i>1
    s = ftell(fid);
    if s>c
        break;
    else
```

```

data = fread(fid,SegLength,'float32'); % Reading file in segment length
Det = data(1); % getting detector value
tgate = data(2); % getting tgate no.
j = 1; k = 1;
plength = 0;
    % finding magnitude in tissues
    for j = 1:Ntissue
        lenTissue = mua(k)*data(j+2);
        plength = plength+lenTissue;
        k = k+1;
    end
end
mag = exp(-plength);
mag = mag/(Nphoton*t*Pi*rad^2);
a(Det+1,tgate+1) = a(Det+1,tgate+1)+mag; % loading magnitude to each location
end

fclose(fid);

% converting 2D matrices into 3D matrices
for k = 1:Ngate
    m = 1;
    for I = 1:det_x
        for j = 1:det_y
            x(i,j,k) = a(m,k);
            m = m+1;
        end
    end
end

% Converting time gated sequence to CW
% cw = zeros(det_x, det_y, Ngate);
% for k = 1:Ngate
%     for i = 1:det_x
%         for j = 1:det_y
%             cw(i,j,k) = x(i,j,k)+cw(i,j,k)
%         end
%     end
% end

fid = fopen('2mm_bile_ref.bin','w'); % Open a file to write
for k = 1:Ngate
    for i = 1:det_x
        for j = 1:det_y

```

```
        fwrite(fid,x(i,j,k),'double'); % writing file
    end
end
end
fclose(fid);
```

MATLAB code for generating a ratio file

```
clear all;
close all;
clc;

fid = fopen('bg_all_ref.bin','r'); % Open background file
fid1 = fopen('2mm_bile_ref.bin','r'); % Open with bile duct file

% Reading files
for k=1:50
    A = fread(fid1,[31,31],'double');
    B = fread(fid,[31,31],'double');
    x(:,:,k) = A;
    y(:,:,k) = B;
end

% Replacing zeros with a nonzero number
for i = 1:31
    for j = 1:31
        for k = 1:50
            if (x(i,j,k) == 0)
                x(i,j,k) = 0.0001;
            end
            if (y(i,j,k) == 0)
                y(i,j,k) = 0.0001;
            end
        end
    end
end

fid2 = fopen('Divide2mm_bile_ref.bin','w');

for k = 1:50
    for j = 1:31
        for i = 1:31
            z(i,j,k) = x(i,j,k)/y(i,j,k);
            fwrite(fid2,z(i,j,k),'double');
        end
    end
end
end
fclose(fid);
fclose(fid1);
fclose(fid2);
```

MATLAB code for fitting “Lorentzian Function”

```

clear all;
close all;
clc;

% reading all files
n = 1;

for I = 1:50
    filename = ['Divide' num2str(12) 'mm_bile_ref_', num2str(i), '.txt'];
    name = [filename];
    A = load([name]);
    x = A(:,1);
    y = A(:,2);
    y = 1-y; % inverting the curve

    % curve fitting
    opts = fitoptions('a/(2*pi)*(c/((x-b)^2+(0.5*c)^2)')); % Lorentzian function
    opts.Lower = [0 -inf 0 0 -inf 0];
    opts.StartPoint = [13 13 4]; % initial guess
    ftype = fitype('a/(2*pi)*(c/((x-b)^2+(0.5*c)^2)');
    [fitting,gof] = fit(x,y,ftype,opts); %fitting performed

    % Confidence limit
    limit = confint(fitting); % confidence limit in rows
    height(:,n) = limit(:,1); % limit for a
    width(:,n) = limit(:,3); % limit for c
    center(:,n) = limit(:,2); % limit for b

    % Fitting values
    a_matrix(n) = fitting.a; % fitted a
    b_matrix(n) = fitting.b; % fitted b
    c_matrix(n) = fitting.c; % fitted c

    % Calculation of error in each term
    err_a(n,:) = a_matrix(1,n)-height(1,n); % std error in a
    err_b(n,:) = b_matrix(1,n)-center(1,n); % std error in center
    err_c(n,:) = c_matrix(1,n)-width(1,n); % std error in FWHM
    cont(n,:) = (2*a_matrix(n))/((pi)*(c_matrix(n)));
    err_pr(n,:) = cont(n,:)*sqrt((err_a(n,)/a_matrix(n))^2+(err_c(n,)/c_matrix(n))^2);
    n = n+1;
end

```

```
x = 1:50;
d = {'x','contrast','std contrast','center','std center','FWHM','std width'};
% Writing values in excel sheet
xlswrite('A.xls',d,'A1:G1');
xlswrite('A.xls',x,'A2:A51');
xlswrite('A.xls',contrast,'B2:B51');
xlswrite('A.xls',err_pr,'C2:C51');
xlswrite('A.xls',b_matrix,'D2:D51');
xlswrite('A.xls',err_b,'E2:E51');
xlswrite('A.xls',c_matrix,'F2:F51');
xlswrite('A.xls',err_c,'G2:G51');
```

APPENDIX B
CONFIGURATION FILE

```

nphotons = 150000000;
seed = 393571066;
freq = 0;

;; Source position. All lengths in mm

source { pos = [ 54 54 1 ] dir = [ 0 0 1 ] rad = 45 } ;

;; Times are in seconds.

start_time = 0.00e-9
gate_width = 0.03e-9 ;; simulations covers a range of 50*0.03 = 1.5 ns
;; gate_width = 0.3e-9 ;; simulations covers a range of 50*0.3 = 15 ns
ngate = 50

segfile bile_2mm.bin ;; segmentation file to load

dx 1 ;; Voxel size. Square voxels only, for now (dz = dy = dx)

nxvox = 100 ;; Size of system in x direction (in voxels)
nyvox = 100 ;; Size of system in y direction (in voxels)
nzvox = 20 ;; Size of system in z direction (in voxels)

;; Region of interest within system volume (also in voxels)
;; If left out, 2pt file covers entire volume.

image_x 0 99
image_y 0 99
image_z 0 19

tissue { mua = 5.19e-3 mus = 1.133 g = 0.01 n = 1.4 } ; optical properties of adipose
tissue { mua = 0.3 mus = 0.625 g = 0.01 n = 1.4 } ; optical properties of bile

;; defining detector position, direction and radius
detector { pos = [ 39 39 1 ] dir = [ 0 0 1 ] rad = 0.5 }
detector { pos = [ .. .. ] dir = [ 0 0 1 ] rad = 0.5 }
detector { pos = [ .. .. ] dir = [ 0 0 1 ] rad = 0.5 }
.
.
.
detector { pos = [ .. .. ] dir = [ 0 0 1 ] rad = 0.5 }
detector { pos = [ 69 69 1 ] dir = [ 0 0 1 ] rad = 0.5 }

```


REFERENCES

1. http://www.emedicinehealth.com/gallstones/article_em.htm.
2. http://mse.mef.hr/msedb/slike/p06030101_1/dir388/pdf0.pdf.
3. R. S. B. Chamberlain, L. H., "Hepatobiliary surgery, CHAPTER 1: Essential Hepatic and Biliary Anatomy for the Surgeon," p. 287, 2003.
4. http://www.pueblo.gsa.gov/cic_text/health/gallstones/gallstns.htm
5. B.W. Trotman, R.D. Soloway, "Pigment gallstone disease: summary of the 6. National Institute of Health-International Workshop," *Hepatology*, 2, 879 (1982)
6. <http://healthlink.mcw.edu/article/950732863.html>
7. Bruce W. Trotman, J. Donald Ostrow, Roger D. Soloway "Pigment Vs Cholesterol Cholelithiasis: Comparison of stone and Bile Composition," *The American journal of digestive Diseases*
8. <http://www.medicinenet.com/gallstones/page2.htm>
9. L. W. Way, L. Stewart, W. Gantert, K. Liu, C. M. Lee, K. Whang, and J. G. Hunter, "Causes and prevention of laparoscopic bile duct injuries: analysis of 252 cases from a human factors and cognitive psychology perspective," *Ann Surg*, vol.237, pp. 460-9, Apr 2003.
10. M. Shaun McKenzie, Richard Schwartz, MD, "The Management of Bile Duct Injuries Occurring During Laparoscopic Cholecystectomy," *Current Surgery*, vol.63, pp. 20-23, 1/2006 2006.
11. http://www.disability.vic.gov.au/dsonline/dsarticles.nsf/pages/Gall_bladder_removal?opendocument
12. <http://adam.about.com/encyclopedia/Gallbladderremoval.htm>
13. http://www.revolutionhealth.com/articles/gallstones/hw107151?ipc=B00519§ion=section_12

14. David R. Flum et al. "Intraoperative Cholangiography and Risk of Common Bile Duct Injury," JAMA, 2003; 290(4):459.
15. John Baillie, Erik Paulson, Kenneth Vitellas "Biliary Imaging: A Review," Gastroenterology 2003;124:1686–1699
16. T. B. Hugh, "New strategies to prevent laparoscopic bile duct injury—surgeons can learn from pilots," Surgery, vol. 132, pp. 826-35, May 25 2002.
17. L. W. Way, L. Stewart, W. Gantert, K. Liu, C. M. Lee, K. Whang, and J. G. Hunter, "Causes and prevention of laparoscopic bile duct injuries: analysis of 252 cases from a human factors and cognitive psychology perspective," Ann Surg, vol.237, pp. 460-9, Apr 2003.
18. Flum DR, Koepsell T, Heagerty P, Sinanan M, Dellinger EP, "Common bile duct injury during laparoscopic cholecystectomy and the use of intraoperative cholangiography: adverse outcome or preventable error?," Arch Surg, 2001. 136: p. 1287-92.
19. Mirizzi. P, "Operative Cholangiography," Surgery Gynecology & Obstetrics, 1937. 65: p. 702-10.
20. D. R. Flum, E. P. Dellinger, A. Cheadle, L. Chan, T. Koepsell, "Intraoperative cholangiography and risk of common bile duct injury during cholecystectomy," Jama, vol. 289, pp. 1639-44, Apr 2 2003.
21. Csendes, P. Burdiles, J. C. Diaz, F. Maluenda, O. Korn, E. Vallejo, P. Csendes, "Prevalence of common bile duct stones according to the increasing number of risk factors present. A prospective study employing routinely intraoperative cholangiography in 477 cases," Hepatogastroenterology, vol. 45, pp. 1415-21, Sep-Oct 1998.
22. E. H. Livingston, J. A. Miller, B. Coan, R. V. Rege, "Costs and Utilization of Intraoperative Cholangiography," J Gastrointest Surg, Jun 30 2007.
23. Huang D, Swanson EA, Lin CP, Schuman JS, Stinson WG, Chang W, et al., "Optical coherence tomography" Science 1991; 254:1178-81.
24. Poneros JM, Tearney GJ, Shiskov M, et al., "Optical coherence tomography of the biliary tree during ERCP" Gastrointest Endosc 2002; 55:84-88.
25. Zuccaro G, Gladkova N, Vargo J, Feldchtein F, Zagaynova E, Conwell D, et al., "Optical coherence tomography of the esophagus and proximal stomach in health and disease" Am J Gastroenterol 2001; 96:2633-9.

26. Pier Alberto Testoni, Benedetto Mangiavillano, Alberto Mariani JOP. J Pancreas, "Optical Coherence Tomography for Investigation of the Pancreatico-Biliary System: Still Experimental?" (Online) 2007; 8(2):156-165.
27. Gurnani, P., "Near Infrared spectroscopic measurement of human and animal brain structures, in Bioengineering", 2003, University of Texas at Arlington. p. 180.
28. Chance B, Nioka S, Kent J, McCully K, Fountain M, Greenfield R, Holtom G, "Time resolved spectroscopy of hemoglobin and myoglobin in resting and ischemic muscle", Anal. Biochem, 1988. 174: p. 698-707.
29. S. L. Jacques, L. Wang, "Monte-Carlo Modeling of Light Transport in Tissues" in Optical-Thermal Response of Laser Irradiated Tissue, A. J. Welch and M. C. J. van Gemert (Plenum, New York 1995).
30. M. K. S. A. Prahl, S. L. Jacques, A. J. Welch, "A Monte Carlo Model of Light Propagation in Tissue," SPIE Institute Series, vol. 1S pp. 102-111, 19195.
31. David Boas, J. Culver, J. Stott, and A. Dunn, "Three dimensional Monte Carlo code for photon migration through complex heterogeneous media including the adult human head" Optics Express, Vol. 10, Issue 3, pp. 159-170.
32. Loening AM, Gambhir SS, "AMIDE: A Free Software Tool for Multimodality Medical Image Analysis", Molecular Imaging, 2(3):131-137, 2003.
33. David A. Soltysik, Kyung K. Peck, Keith D. White, Bruce Crosson, Richard W. Briggs, "Comparison of hemodynamic response nonlinearity across primary cortical areas", NeuroImage 22, 1117- 1127 (2004).
34. www.wikipedia.com
35. <http://www.rxlist.com/cgi/generic/intralipid20.htm>

BIOGRAPHICAL INFORMATION

Nimit Patel was born on May 15th, 1984 in Ahmedabad, Gujarat, India. He graduated with a Bachelor's in Biomedical & Instrumentation Engineering from U.V. Patel College of Engineering, North Gujarat University, India in June 2006. He then worked as a visiting faculty for six months at the Government Engineering College in Gandhinagar, Gujarat. After that he joined the Master of Science program in Bioengineering at the University of Texas at Arlington in Spring 2007. After a semester of study he found medical optical imaging an interesting and emerging field for research and then he was bent on doing research in the same. He started working as a Graduate Research Assistant in medical optics laboratory in May 2007. Apart from his current research (Time resolved optical imaging); his interest lies in Fluorescence imaging, NIR spectroscopy and Image processing and Biomedical Instrumentation for developing non-invasive systems for clinical use.